ABSTRACT

KIM, JAEWOO. Shape Synthesis and Fundamental Limits of Complex-Structured Dielectric Resonator Antennas - (Under the direction of Dr. Jacob J. Adams).

Dielectric resonator antennas have received a lot of interest over years. Though various DRAs have been proposed in the literature, there has been little investigation of DRAs having arbitrary shape since fabricating a high permittivity material is technically difficult due to its hardness and brittleness. However, a recent advancement of 3D printing technique makes it possible to fabricate a complex structured DRA with high permittivity material in micro-meters. Based on this, we investigate complex-structured DRAs and their fundamental limits. Then we design a complex structured MIMO DRA by using the limits and a novel shape synthesis method.

The thesis consists of two major chapters. First, we investigate the physical bounds on DRAs confined within a volume to show that eigenmodes of DRA substructures cannot have lower resonant frequency or Q-factor than the eigenmodes of their superstructure. Following recent theoretical results, we study the shape optimization of several DRAs to minimize their Q factor or resonant frequency. A MoM based in-house code using Genetic algorithm(GA) and Characteristic mode analysis(CMA) synthesizes the antenna shape to lower Q-factor or resonant frequency. The simulation results show the lowest Q-factor and resonant frequency of the dielectric substructures are converged to the values of the complete structure, confirming prior theoretical bounds.

Second, a rectangular DRA structure is synthesized by the same optimization code to resonate three different modes at 2.45GHz by *shape-first feed-next* methodology. The objective of this chapter is to introduce a novel design procedure for MIMO DRAs with arbitrary shape. Based on the lower bound of the resonant frequency, the dimension of the rectangular structure is chosen to resonate its third characteristic mode lower than 2.45GHz and the structure is optimized by the in-house code. As a feeding method, the ports of the optimized structure are fed by a pair of slots,

a slot and a coaxial probe. Then the antenna structure is manually updated before fabrication to prevent errors in measurement. The simulation results show the reflection coefficient and coupling of DRA MIMO antenna are lower than -22dB and -38dB at 2.45GHz. Each port has 6.53dB, 6.36dB and 3.47dB of directivity. Drawbacks of the antenna are the narrow bandwidth(20MHz at -10dB) and the large size of the antenna due to the stub matching.

Shape Synthesis and Fundamental Limits of Complex-Structured Dielectric Resonator Antennas

by
Jaewoo Kim

A thesis submitted to the Graduate Faculty of
North Carolina State University
in partial fulfillment of the
requirements for the degree of
Masters of Science

Electrical Engineering

Raleigh, North Carolina
2021

APPROVED BY:

_____	_____
Dr. Jacob J. Adams Committee Chair	Dr. Brian A. Floyd
_____	_____
Dr. David S. Ricketts	Dr. Binbin Yang

DEDICATION

This thesis is dedicated to all my family, who have supported and loved me for years. Especially, I would like to express my deepest appreciation to my wife, Songah, and daughter Seoha.

BIOGRAPHY

Jaewoo Kim was born in Daegu, Korea in 1992. He received his Bachelor's degree in Physics Science from Korea Military Academy, Seoul, Korea in 2015. He serves for Korean Army as an officer and pursed his master's degree at North Carolina State University, Raleigh, NC, USA.

He studied at Antenna and Electromagnetics Lab under Dr. Jacob J. Adams. His research interests include DRA, MIMO antennas and characteristic mode analysis.

ACKNOWLEDGMENTS

I would like to thank my advisor in my master's education, Dr. Adams, who has exceeded all possible expectation of an advisor. His advice, knowledge and encouragement broaden my sight and he help me explore a lot of academical experience.

I would like to thank Dr. Yang for all collaboration and leading the research work. As a pioneer on my research subject, his knowledge and advice helped me experience a higher level of research work.

I also would like to thank Korea Army. Thanks to offering the chance to study abroad, I have achieved a lot of valuable experience in U.S. They have supported me in many ways for last two years. I sincerely express my appreciation for all the supports.

At last, I would like to thank my wife, Songah Koo. Without her endless sacrifice and support, it was impossible finishing the degree.

TABLE OF CONTENTS

LIST OF TABLES

LIST OF FIGURES

CHAPTER 1 : Introduction

The concept of using dielectric material for a resonator was first introduced by Richtinger[1] in 1930 and Okaya and Barash first analyzed the mode in the dielectric cavity in the early 1960s [2]. The initial dielectric resonators had a cylindrical shape and relatively high dielectric constant($\varepsilon_r > 35$) to keep the compactness[3]. Over time, the dielectric resonator antenna(DRA)s have a significant interest due to their benefits in the following section and there have been a lot of research papers representing diverse DRAs. The papers have covered the wide ranges of DRA operating frequency(55MHz < f <94GHz) and dielectric constant(8<ε_r<100) and have introduced diverse shapes of DRAs : cylindrical[4] to rectangular[5], hemisphere[6] and triangular[7]. However, fewer fields of DRA have been explored and there is still a lack of information about the DRA's characteristics compared to the metallic antennas.

As part of research investigating the characteristics of DRA, the thesis has two objectives. The first objective is to investigate DRA's fundamental limits about the quality factor and resonant frequency. A lower bound on quality factor of the metallic antennas was already published and it is expanded to DRA with a mathematical proof in a recent research paper[8, 9]. And the paper also includes a lower bound on the resonant frequency of DRA. We briefly introduce the mathematical proofs of lower bounds and support them with some numerical examples here. When it comes to designing an antenna, the bandwidth and resonant frequency are key considerations as these are important performance metrics. Therefore, the investigation of the lower bounds will give better insight and guidance to antenna designers.

The second objective is to suggest a new design process for a complex-structured MIMO DRA via a design example. We use the fundamental limits and apply a shape synthesis method based on a prior work of planar metallic antenna to DRA. Only one case is coved in the thesis, but

it can be applied to the other designs with different frequencies and permittivities. Since the thesis includes detailed steps from choosing the resonant frequency to feeding technique and the fabrication procedure for DRA MIMO, the whole process would provide an insight for choosing antenna specifications and designing the antenna.

1.1 Overview of Thesis

The thesis is organized into four logical chapters to cover DRA physical limitation and feeding technique for DRA MIMO. Chapter 1 covers the introduction and literature review, which covers MIMO, DRA and the related theory. Its definition, recent research, characteristics and limitations are introduced in this chapter.

Chapter 2 focuses on the physical limitation of DRA. The idea is to verify the possibility of improving Q-factor and resonant frequency with a substructure of DRA. The idea is mathematically proved for metallic antennas in [8] and expanded to DRA considering its capacitive nature. The mathematical proofs are briefly introduced and supported by some numerical examples with optimization results. The results show how Q-factor, resonant frequency and the antenna structure change under a specific cost function.

In Chapter 3, DRA rectangular structure is optimized by the same code with a different cost function to resonate multiple characteristic modes. With the optimized structure, two feeding techniques are introduced and compared. After then, the fabrication procedure is introduced before 3D printing antenna structure. The final simulation result is presented.

Chapter 4 summarizes the overall thesis and represents the main contribution of the thesis. Also, the chapter introduces some limitations and future works.

1.2 Dielectric Resonator Antenna(DRA) benefits

This section introduces some benefits of DRA. First, the main benefit used for the thesis is that the currents are distributed over the dielectric volume and it potentially allows additional modes that wouldn't be exist in a metallic antenna. Second, the wavelength of free space is reduced by $\sqrt{\varepsilon_r}$ in a dielectric material, making the DRA size proportional to $\lambda/\sqrt{\varepsilon_r}$. Third, DRA has a high radiation efficiency since the conducting loss in dielectric material is much less than that in the metallic material [10,11]. The last advantage is that DRA has flexibility for a design. The antenna structures can be designed and printed in different geometries by additive manufacturing techniques. Also, it can be excited by different feeding techniques in the fabrication process, such as microstrip line[12, 13], coaxial feedline[14,15], probe[16], slotline[17], etc. The designer can choose one of these different excitation methods to suit the purpose and control each characteristic of DRA easily. Based on the benefits, the dielectric materials have been used for various purposes such as low-profile, broadband, MIMO and the thesis mainly covers MIMO DRA.

1.3 MIMO system

The concept of MIMO was first proposed by Foschini, Gans and Telatar in the 1990s by [18], [19] to improve wireless capacities and to deliver higher bit rates efficiently. The main idea of the MIMO system is to implement multiple antennas at both transmitter and receiver.

Figure 1.1 represents that the transmitted signals reach to the receivers through multiple paths. The MIMO system has M transmitters and N receivers, creating M×N propagation paths. Each of M or N elements can be divided in different antenna elements like array antennas and they can be in one antenna elements by using multi-ports. The multiple elements enable to send multiple data streams simultaneously that can be separated by spatial multiplexing.

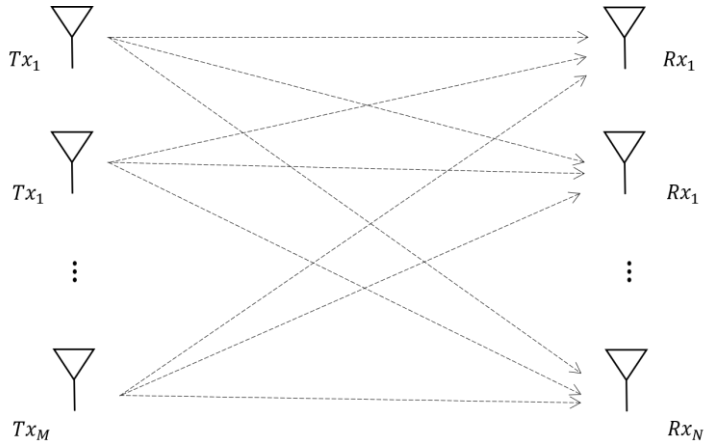

Figure 1.1: Basic structure of MIMO system

The spatial multiplexing is one of the key techniques of the MIMO system and offers a linear increase of data capabilities. It indicates sending distinct data streams over the different channels simultaneously by using multiple transmitters and receivers. It subsequently increases the data capacity. The number of data streams equals the minimum number of the transmit/receive antennas(min$\{M_{trans}, N_{receiver}\}$) and each data stream experiences at least the same channel quality with that of the SISO antenna[20].

However, MIMO antennas also have a fundamental challenge due to the spatial constraint in practice. Generally, the minimum Q factor of antenna increases with the size of antenna due to the lower bound of Q factor. It was firstly introduced by Chu's paper and a recent paper demonstrated that Q-factor of a metallic substructure is bounded by the minimum Q-factor of the full-volume structure [8, 21]. This lower bound is applied to metallic antennas and the limit on DRA is covered in a later chapter. Besides, the closer elements in array MIMO antennas increase the interaction, known as mutual coupling[22]. The coupling not only reduces the radiation efficiency but also affects the correlation[23]. A high level of correlation usually occurs with high mutual coupling[9] and yields a low capacity of MIMO[23].

To overcome the challenge of compact MIMO antenna design, there has been diverse research in multiple perspectives. Over the last few decades, many researchers have tried to reduce the mutual coupling of MIMO antennas by using isolation techniques such as connecting transmission lines[25], systemically designing decoupling network from the matrices calculation[26,27], using electromagnetic band-gap(EBG) structure[28,29], using parasitic element[30], etc.

One interesting subject of the research field is designing the compact MIMO antenna. One suggestion is using dielectric material as a resonator since the wavelength of free space is reduced by $\sqrt{\varepsilon_r}$ (ε_r: $dielectric\ constance$) in a dielectric material, which implies DRA have $\frac{1}{\sqrt{\varepsilon_r}}$ of the antenna size compared with the metallic antenna in the same condition.

1.4 MIMO DRA

The applications of DRA have been expanded over recent years. One of the applications is using a dielectric material for a resonator of MIMO antennas. To design MIMO DRA, many researchers have studied isolating antenna elements with orthogonal mode generation[31], defected ground structure[32], metallic strip or parasitic elements [33], or a combination of techniques[34]. Several research papers reported dual-polarized MIMO DRA [35,36] and some other research used multiple DRA elements like array antennas to resonate more than two modes[37]. However, despite the techniques, resonating more than two modes with a single dielectric resonator is not straightforward. Recently, some studies have introduced DRA MIMO resonating three modes[4,38-39] through a single DRA element. Figure 1.2 and Table 1.1 show pictures and the performance of these three mode DRAs.

Table 1.1: Examples of 3 ports MIMO DRA

	Antenna shape / size (wavelength in material)	Operating frequency (Wave length)	Dielectric constant	Reflection Coefficient	coupling	Fractional Bandwidth
[4]	Cylindrical Radius: 0.67λ Height : 0.8λ	2.45GHz (39.11mm)	9.8	<-22dB	<-24dB	100MHz
[38]	Rectangular $3.2\lambda \times 1.77\lambda \times 1.34\lambda$	9.48GHz (9.9mm)	10.2	-10~-30	<-20dB	720MHz
[39]	Rectangular $1.16\lambda \times 1.16\lambda \times 0.9\lambda$	2.45GHz (26.72mm)	21	-10~-20dB	-11~-15dB	100MHz

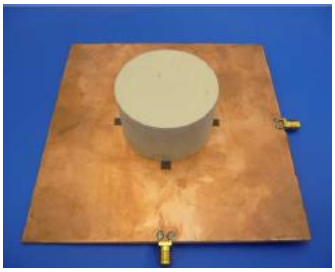

[7]

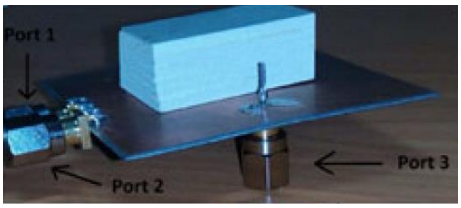

[44]

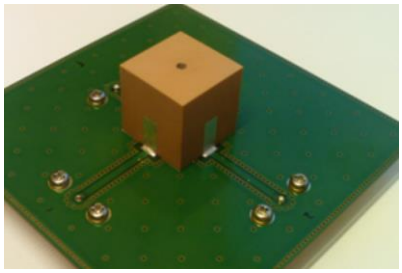

[45]

Figure 1.2: MIMO DRA examples

All three references showed results with different permittivities, feeding methods and antenna shapes. Also, the results imply a trade-off between bandwidth, radiation efficiency and effective size of the antenna. Comparing the wavelength in a dielectric material, [38] has an electrically large size with a good coupling value and [39] has a slightly higher coupling value with the electrically smaller size. Reference [4] has a similar size to [39] and shows good efficiency with narrower bandwidth than [38]. However, in terms of the shape, they are not out of the conventional shapes. One practical reason for canonical shapes is that the traditional milling method had a limitation in fabricating the complex-shaped structure with high permittivity due to cost and difficulty.

On the other hand, the dielectric resonator in the thesis will have an intricate shape because it will be optimized by a shape optimization method. The optimization process divides the dielectric structure into many tetrahedra and removes some of them, subsequently making a complex shape with sharp edges and vertices. Due to the high permittivity and complex shape, conventional technology cannot easily fabricate the antenna structure. Therefore, the thesis addresses the problem with the 3D printing technique, attracting a lot of interest recently.

1.5 3D Printing(Additive Manufacturing)

In the late 80s to early 90s, technologies of 3D printing such as Selective Laser Sintering(SLS), Fused Deposition Modeling(FDM) were developed and started to be employed in the industrial areas in the early 2000s[40]. Since then, 3D printing has attracted significant interest from various areas such as automobile, robotics, biomedical field due to its benefits of low cost, high accuracy, light weight, time-efficiency and environment-friendly [41]. The microwave field also employed 3D printing technology, however, most printed works were polymer-based materials with low permittivity ($\varepsilon_r < 4$) since high permittivity materials are difficult to fabricate due to their hardness and brittleness [42-44]. Considering the permittivity range used in research, a permittivity between 8 to 100 is considered a suitable value for use in dielectric resonator and more printed works with high permittivity materials are needed.

As 3D printing technology has advanced, it allows printing of the high permittivity material like ceramic and opens the possibility of rapid prototyping of complex-shaped DRA [45-47]. Figure 1.3 shows some printed antenna structures with complex shapes from recent research. Structures in (a) and (b) are printed by Fused deposition modeling(FDM) method. The resolution and accuracy are mainly decided by the nozzle diameter, normally $250{\sim}400\mu m$ in the FDM

method. The printed material of (a) is Polylactic acid(PLA) added with graphite fibers, called a conductive PLA in reference[47]. It exhibits a conductivity of $10^2 S/m$ and dielectric constant of 6.41 with dimension of $125 \times 125 \times 165 mm^3$. Loss tangent is negligible. The structure in (b) uses Premix material having $40 \times 40 \times 20 mm^3$ of dimension and 7.5 of permittivity [48]. The structure in (c) is printed by Stereolithography(SLA) which has higher accuracy, resolution and surface finishing than FDM by allowing a lower layer thickness value. Epoxy resin with 3.6 of permittivity is widely used for this method.

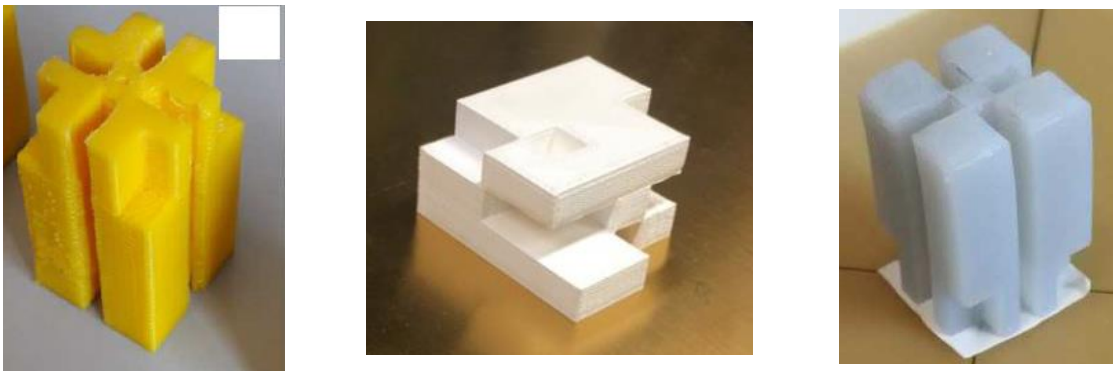

(a) [47] (b) [48] (c) [47]

Figure 1.3: Examples of printed structures

Besides the nozzle size, the resolution and accuracy of the printing method vary depending on the type of printing technology and the printed material. (normally $mm \sim \mu m$, $20 \mu m$ in this research). Materials with higher permittivity usually require more advanced technology to print accurately. Even though the above references used permittivity lower than 10, new emerging technologies bring new methods to print high permittivity material such as ceramic. One research paper shows a ceramic structure printed with 0.43 μm of resolution by micro-ceramic stereolithography(μCSL) after photocuring activity at UV irradiation [49]. Besides, another research printed high permittivity material($\epsilon_r > 20$) with less than 100 μm of accuracy[50,51].

Based on the printed examples and recent achievements in 3D printing technology, it is expected that the designed DRA in this paper will be accurately printable.

CHAPTER 2 : Physical Limitation on Substructure of DRA

2.1 Objective

This chapter introduces fundamental limitations of DRAs, with regards to their Q-factor and the resonant frequency. New lower bounds for these two characteristics were recently proposed [9] and will be demonstrated by numerical examples. In particular, the bounds on a DRA are similar to those proposed of a metallic antenna's [8], in that the Q-factor of any substructure is bounded from below by the Q-factor of a bounding superstructure. A substructure is defined by removing some parts from the superstructure. Besides the lower bound of the Q factor, the capacitive nature of DRA modes introduces a new bound on the lowest resonant frequency possible with a DRA, showing that no sub-structure can have a lower fundamental resonance than the superstructure.

In the chapter, the mathematical proofs of these lower bounds are briefly presented to explain the theoretical background. Then, the shape synthesis is performed by the optimization code based on characteristic mode analysis(CMA) and genetic algorithm(GA). This code enforces a rectangular(complete) structure to have the best shape by removing parts according to the cost function, which minimizes the Q-factor or resonant frequency in this chapter. The optimization results will demonstrate and support the theoretical proofs. Besides, presenting the optimization result and how the structure changes with generations will give an insight into the relationship between the bounding and antenna structure. Furthermore, as minimizing antenna size with keeping the performance is important for the next generation of the wireless communication, the research result could provide a design consideration of miniature DRA.

2.2 Theoretical Background

2.2.1 Characteristic Mode Theory(CMT)

Characteristic mode theory was first introduced by Garbacz [52] and improved by Harrington [53] and widely used to analyze the arbitrary shape of conducting body. One of the advantages of CMT is decomposing the full-wave solution into individual characteristic modes. Since each characteristic mode has orthogonal current distributions and far-field patterns, it allows the investigation of each characteristic mode of the antenna structure and helps to understand how Q-factor and resonant frequency change with the structure. According to the notation in Harrington's paper[53], the characteristic modes are solutions of the following eigenvalue equation of radiating object.

$$XI_n = \lambda_n R I_n \tag{1}$$

Where R and X are real and imaginary parts of Z matrix and both are real symmetric operators, which are generated by the method of moments(MoM)[54]. λ_n and I_n are eigenvalue and eigencurrent(or characteristic current) of the n-th mode, having real values. The order(n) of characteristic mode is used to correlate eigen solutions at one frequency to other eigen solutions at different frequencies, called modal tracking. By sorting the modes, we can investigate the resonant behavior of each mode over a wideband. As outcomes from equation (1), two important parameters are obtained as following: eigenvalue (2) and modal significance(MS_n) (3).

$$\lambda_n = \omega \iiint (\mu |H_n|^2 - \epsilon |E_n|^2) dV \tag{2}$$

$$MS_n = \frac{1}{|1 + j\lambda_n|} \tag{3}$$

Both parameters are directly related to the reactive energy of the antenna. Once the stored electric energy dominates the stored magnetic energy, the antenna is capacitive and the eigenvalue has a negative value. On the other hand, in the case of $\lambda_n > 0$, the antenna becomes inductive and the stored magnetic energy dominates the stored electric energy. When $\lambda_n = 0 (MS = 1)$, the stored electric energy and the stored magnetic energy cancel each other and the mode of the antenna is self-resonant.

Another important parameter is Q factor that is inversely proportional to the bandwidth of antennas. It is defined as the ratio of the stored energy to the dissipated energy and a recent paper [55] calculated Q factor of a characteristic mode via the energy terms. The calculation for arbitrary DRA is represented in [56] as following equations (4)-(7). W_n^e and W_n^m represent the stored electric and magnetic energy, P_n^{rad} denotes the radiation power of n-th mode. I_n , X_n^e and X_n^m represent a modal current, stored electric energy and stored magnetic energy.

$$Q_n(I) = \frac{2\omega\{W_n^e, W_n^m\}}{P_{rad}} = \frac{max\{I_n^H X_n^e I_n, I_n^H X_n^m I_n\}}{I^H R I} \tag{4}$$

$$W_n^e = \frac{1}{4\omega} I_n^H X_n^e I_n \tag{5}$$

$$W_n^m = \frac{1}{4\omega} I_n^H X_n^m I_n \tag{6}$$

$$P_n^{rad} = \frac{1}{2} I_n^H R I_n \tag{7}$$

2.2.2 Capacitive Nature of DRA

Some research papers represent eigenvalue plots of DRA[57,58] by using CMA. By observing the plots, we can obtain some meaningful information about DRA's characteristics such as all eigenvalues have negative values below first resonance. However, a solid mathematical proof

is needed since this observation cannot sufficiently demonstrate the characteristic of DRA regarding the Q-factor and the resonant frequency.

Recently, one research paper mathematically proved the capacitive nature of DRA[9]. Here we briefly introduce the proof. First, the paper used the equations of the stored magnetic energy in free space(W_m^{vac}), stored electric energy in free space(W_e^{vac}) and the stored magnetic energy in material(W_e^{mat}) in [55].

$$W_m^{vac} \approx \frac{k^4}{16\pi\omega^2\epsilon_0}\int_{\Omega_1}\int_{\Omega_2}\left[\frac{J_1^{(1)}(r_1)\cdot J_2^{(1)*}(r2)}{r_{21}}+\frac{c^2}{2}\rho_1(r_1)\rho_2^*(r_2)r_{21}\right]d\Omega_1\Omega_2 \approx C_1k^2 \tag{8}$$

$$W_e^{vac} \approx \frac{c^2k^2}{16\pi\omega^2\epsilon_0}\int_{\Omega_1}\int_{\Omega_2}\left[\frac{\rho_1\ (r_1)\cdot\rho_2^*(r2)}{r_{21}}\right]d\Omega_1\Omega_2 \approx C_2k^0 \tag{9}$$

$$W_e^{mat} \approx \frac{k^2}{4\omega^2\epsilon_0}\int_{\Omega}\left[\frac{J_1^{(1)}\cdot J_2^{(1)*}}{\epsilon_r(r)-1}\right]d\Omega \approx C_3k^0 \tag{10}$$

From the equations of [55], the equations (8) ~ (11) are approximated [9] for the dielectric material. J(r) represents the polarization current, $\epsilon_r(r)$ is the relative permittivity distribution of the dielectric object, Ω is DRA domain, $r_{21} = |r_2 - r_1|$ is the distance between sources. For the approximated equations, the first order limit is assumed to investigate DRA's behavior in an electrically small regime that $\cos(kr) \approx 1$, $\sin(kr) \approx kr$ as $kr \to 0$ where $k = \frac{\omega}{c} = \frac{angular\ frequency}{speed\ of\ light}$ is the phase constant. Then each equation can be represented in terms of k with constantsC_1, C_2 and C_3 as $k \to 0$.

$$I^H ZI \;= I^H RI \;+ jI^H XI \;= 2P_{rad} + j4\omega(W_m^{vac} - W_e^{vac} - W_e^{mat}) \\ = 2P_{rad} + j4\omega(C_1 k^2 - C_2 k^0 - C_3 k^0), \text{ as } k \to 0 \tag{11}$$

$$\lambda_n = \frac{I_n^H XI_n}{I_n^H RI_n} \tag{12}$$

Then the paper used the notation in [59]. $I^H XI$ and $I^H RI$ are expressed as the radiated power and the stored energy of the antenna as shown in equation (11) [59]. In the equation, $I^H XI$ term corresponds to $4\omega(W_m^{vac} - W_e^{vac} - W_e^{mat})$ and it has a negative value as k approaches to zero due to the order of k, meaning all modes are capacitive below the first resonance.

2.2.3 Summary of limitation on DRA substructure

Next, we summarize why substructures of a DRA have a lower bound on the resonant frequency and Q-factor below the first resonance. The substructure is defined by removing certain parts from the structure. By investigating Q-factors and resonant frequencies of the substructure and the complete structure(superstructure), we can study how the size(volume) of the antenna affects these parameters and subsequently obtain insight in designing DRA.

The limitations on Q-factor and resonant frequency of the metallic antenna were previously represented in [8] and the bound of the resonant frequency is recently expanded to DRA [9] as following.

$$\lambda_k \geq \bar{\lambda}_k \geq \lambda_{k+K-\overline{K}}, \qquad 1 \geq k \geq \overline{K} \tag{13}$$

Where λ and $\bar{\lambda}$ are the k-th eigenvalue of the superstructure and substructure, which are solutions of the equation (1). k represents the order of characteristic mode of DRA. K and $\overline{K}$ mean the rank of the Z matrices of the complete structure and the substructure. Considering the capacitive(negative eigenvalue) nature of DRA, equation (13) show that the eigenvalue of the

superstructure must be closer to zero than that of any substructure. Since antennas resonate when the eigenvalue is zero, it also implies the complete structure must have a lower resonant frequency. Thus, characteristic modes of all DRA substructures should have a higher resonant frequency than the superstructure.

The lower bound about Q-factor is proved in the same way. Below the first resonance, due to its capacitive nature, DRA doesn't have inductive mode and the stored electric energy dominates over the stored magnetic energy. Then the limitation on the Q-factor of substructure is represented as (14).

$$Q_k < \bar{Q}_k < Q_{k+K-\bar{K}}, \qquad 1 > k > \bar{K} \tag{14}$$

Q and $\bar{Q}$ indicate Q-factors of the superstructure and the substructure. This equation means the k -th mode of the substructure's Q-factor has a lower bound at the Q-factor of the superstructure. Thus, all substructures have narrower bandwidth than their superstructure below the complete structure's first resonant frequency.

2.2.4 Genetic Algorithm

To calculate Q-factor and the eigenvalue, in this paper, the antenna structure is divided into tetrahedra and analyzed[60] by CMA with many calculations. To address the calculations, we use Genetic algorithm(GA), one of the optimization tools for dealing with electromagnetic problems with a large number of parameters[61, 62].

A binary genetic algorithm is employed in the thesis to synthesize the antenna shape subject to the fitness function. GA code decides whether each tetrahedron is removed(0) or not(1) based

on the fitness function. The below picture and the following steps describe how the code optimizes the structure.

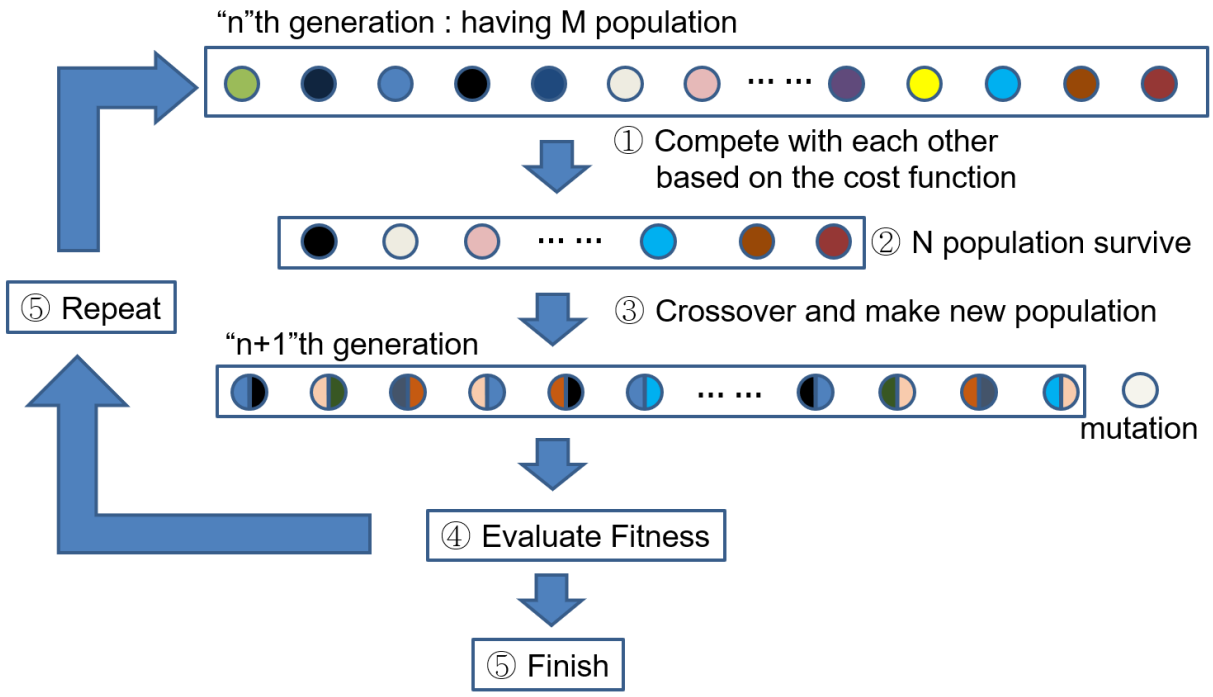

Figure 2.1: Genetic Algorithm

1) Each generation has 40 structures(parent). Structures in the generation have different shapes.
2) Competition between structures, the best structures are chosen under the fitness(cost) function.
3) The next generation is created by crossover from the chosen structure and mutation. The probabilities of crossover and mutation are 50% and 12%.
4) Evaluate the generation based on a cost function.
5) Depending on the fitness result, the optimization is finished or repeated.

2.3 Limitation on DRA structure

To support the mathematical proofs of lower bounds, GA optimization results are introduced here. Following the optimization algorithm in 2.2.4, this antenna structure is optimized by the in-house MoM code based on the SWG basis function [60] and CM solver [63]. The overall shape synthesis procedure follows [64]. The optimization starts with 40 different structures and each structure has random chromosomes (0 or 1), meaning random tetrahedron are removed from the superstructure. Then GA code evaluates how well the structures meet the fitness function and calculates the fitness value of each structure by CMA. Depending on the fitness values, the best 50% of structures survive. The survived structures create a new generation with 12% of mutation and 50% of crossover. Mutation is randomly generated element and crossover is combining and mixing the chromosome of parents. This process is repeated until the fitness of the structure converges to a certain value. During the optimization process, the best fitness value of each generation is recorded and the convergence of these values is shown as an optimization result.

The superstructure in this paper is a rectangular DRA($25 \times 40 \times 16mm^3$) in free space and zirconia is considered as a material having permittivity of 23. The structure is symmetric about x and y axes for simple calculation and optimization. Loss is ignored for CMA. As proved in the last section, it is expected that the first resonant frequency of substructure DRA is bounded by that of complete structure and it also means the eigenvalues of substructure below the first resonance should be a negative value and lower than the supurstructure's.

The first resonant frequency of the complete DRA is 1.95GHz. To observe the possibility of breaking the lower bound of the lowest resonance, 1.2GHz is chosen as optimizing target frequency and the cost function is defined as $-\lambda_n$. It attempts to force substructures to have a

lower eigen value at 1.2GHz to survive in the GA optimization and the resonant frequency over generations subsequently converges to the lowest value.

Figure 2.2 shows the results of the optimized shape, eigenvalue and modal significance and compares them with the results of the superstructure. The first four characteristic modes of the rectangular(complete) structure are chosen for optimization and the optimization for each mode is conducted separately.

(a) shows a convergence of the characteristic eigenvalues of the first four modes of Zirconia DRA at 1.2GHz. The black dotted lines(λ_k) represent the eigenvalues of the complete structure's first four modes at 1.2GHz. $\bar{\lambda}_k$ represents the eigenvalues of substructures. Each mode($\bar{\lambda}_k$) is optimized by completely independent simulations and cost functions in an attempt to lower any of these resonant frequencies below the fundamental resonance of the superstructure at 1.95GHz. Then the optimized results are combined into one plot. As a result, we found that the eigenvalue of each mode increases over generations and they are finally bounded on that of the superstructure. The geometry on the plot represents the final optimized structure of all four modes.

(b) shows MS optimization result of the lowest order mode. The black dotted line represents the MS plot of the complete structure's fundamental mode, which has 1.95GHz of the lowest resonant frequency. Other lines mean MS results of the substructures' equivalent mode at every 5^{th} generation. As shown in the plot, the resonant frequency of the substructure is 3.27GHz at 0^{th} generation and converges to 1.95GHz over generations. After the 25^{th} generations, the MS result of the substructure becomes almost identical with the superstructure and parameters do not change noticeably.

(c) shows how the substructure changes with generations. The structure starts with the arbitrary shape having a much smaller volume than the superstructure. As it is optimized, the

geometry converges to the rectangular(complete) structure. It implies that the substructure needs to be the superstructure to have the lowest resonant frequency.

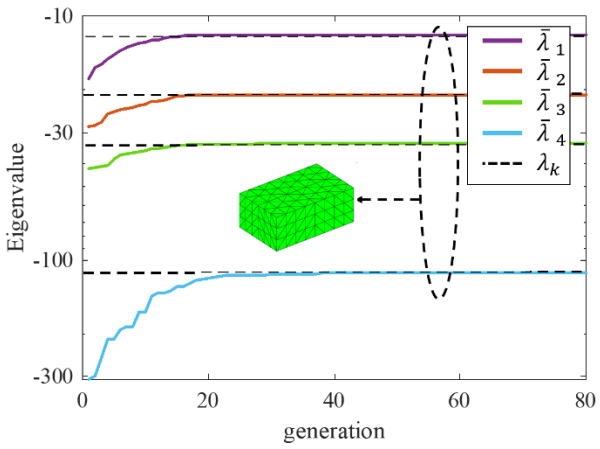

(a)Eigenvalue optimization result

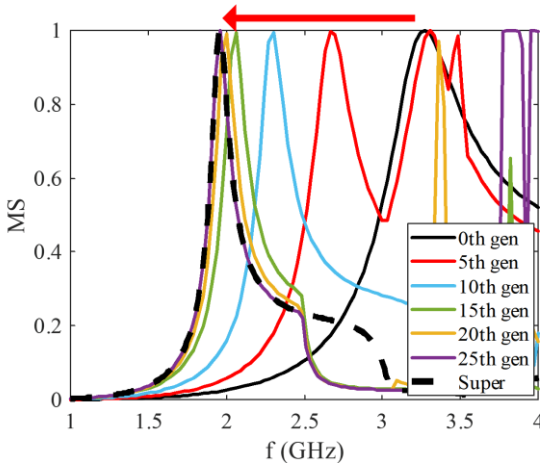

(b) MS optimization result

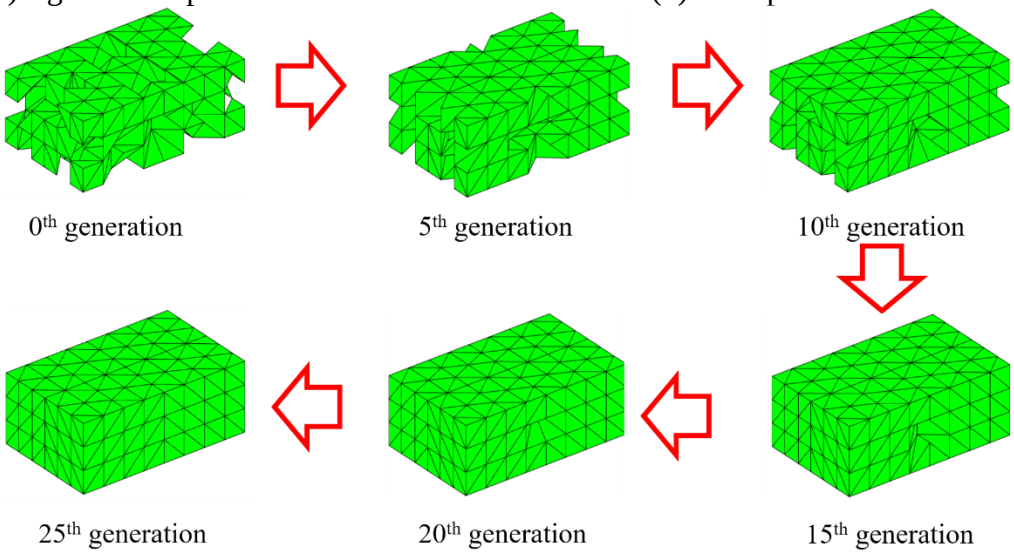

(c) Structure over generations

Figure 2.2: Optimization results of the eigen current, MS and the structure

Figure 2.3 shows the first four modes of the optimization results and the superstructure. CM(super) and CM(opt) represent the characteristic modes of the superstructure and the optimized results. As done in Figure 2.2 (a), each mode is optimized by the completely independent simulation and combined into one plot to investigate four modes simultaneously. Then the final optimized result of each mode is combined into one plot.

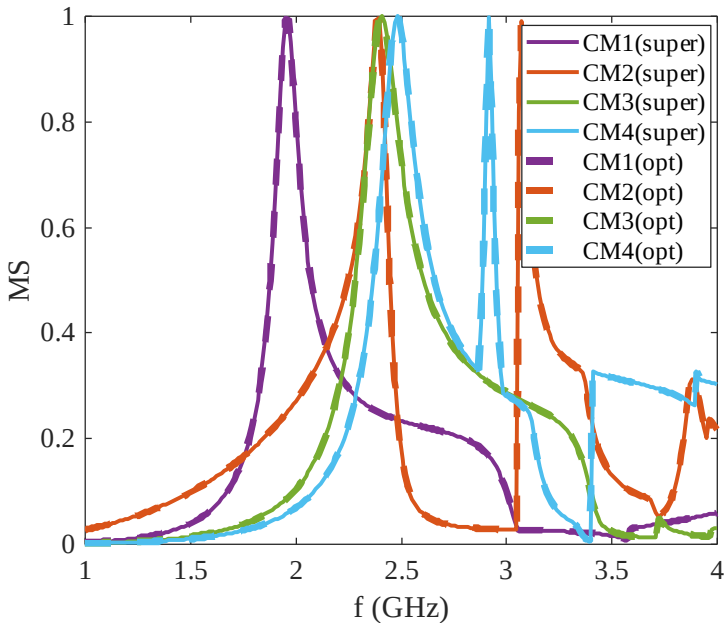

Figure 2.3: Comparing Modal significance of the optimization result and the superstructure

In the same manner, Figure 2.4 represents the optimization results of Q-factors at 1.2GHz. Q_k and $\bar{Q}_k$ represent Q-factor of the superstructure and the substructure. Each $\bar{Q}_k$ is optimized independently with the cost function of $\bar{Q}_k$. By the cost function, the code enforces each mode to have the minimum Q-factor at 1.2GHz. The figure shows Q factors of the substructures decrease over generations and converge to the value of the superstructure. After the 25th generation, substructures have the same Q factor with the complete structure and the parameters do not change noticeably.

Figure 2.5 shows Q-factors of the superstructure and the optimized structures versus frequency over 1~3GHz after the convergence. From the optimizations of Figure 2.4, we obtained four structures and they are analyzed by CMA code to calculate the Q factor. These optimizations and analyses are also independent of each other and combined into a single plot to investigate four

modes simultaneously. As expected, the obtained Q plot from each geometry has the same values with the superstructure over 1~3GHz.

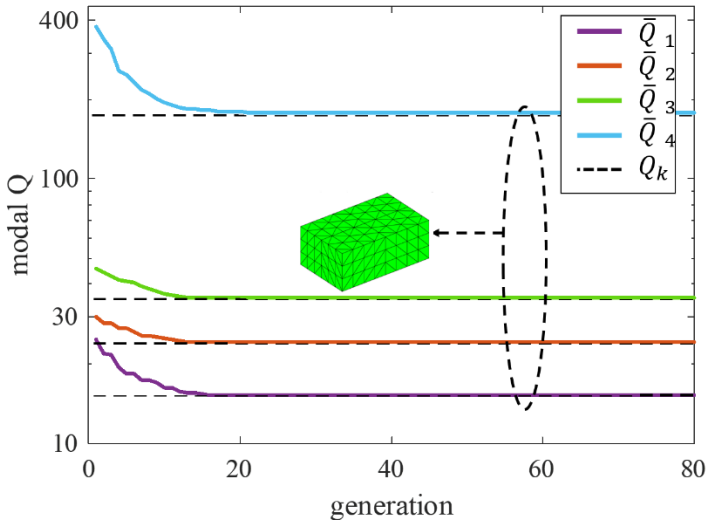

Figure 2.4: Convergence of Q factor

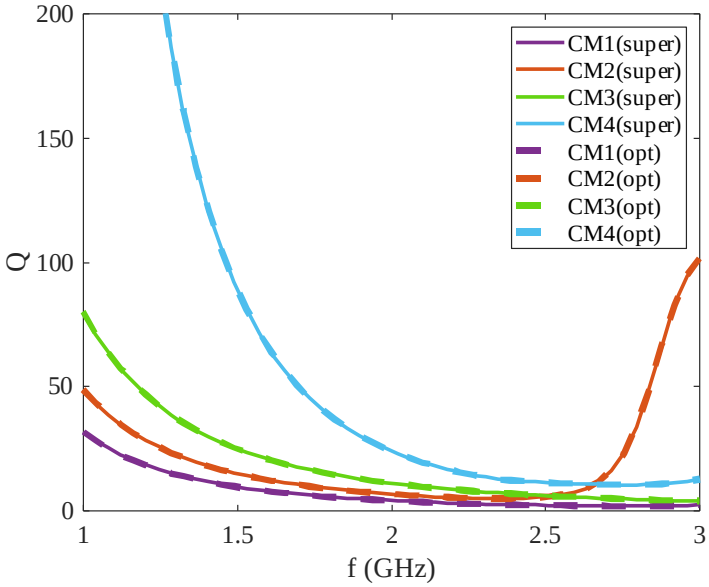

Figure 2.5: Comparing Q-factor of the optimization result and the superstructure

2.4 Discussion

The numerical examples efficiently demonstrate the recent mathematical proof of lower bounds of Q factor and the resonant frequency of DRA substructure. Even though this paper introduces a single superstructure having $25 \times 40 \times 16mm^3$ of dimension and 23 of permittivity, it will also apply to other DRA with different permittivity and geometry. Few other examples are introduced in [9].

This chapter contributes to providing a consideration about DRA's fundamental limitation. As an antenna is designed, we always have a trade-off between antenna size, radiation efficiency and bandwidth. It is impossible to have good radiation efficiency, wide bandwidth and small antenna size simultaneously. However, investigating the lower bounds of DRA aids researchers in choosing the antenna's specification by providing the limits of the Q factor and the resonant frequency.

2.5 Summary

In this chapter, the fundamental characteristic of DRA based on its capacitive nature is introduced. A recent research paper mathematically proved that each characteristic mode of the DRA substructure cannot have a lower resonant frequency than its equivalent mode of the complete structure. Also, below the first resonance of the superstructure, each mode of DRA substructure always has a higher Q-factor than that of the superstructure. Two conjectures are demonstrated by the numerical examples in this chapter. MoM-based GA code optimized substructures of DRA to break the lower bound of the Q factor and the resonant frequency. As a result, the substructures become the superstructure after optimizations and the parameters of the substructure are bounded on the superstructure's values.

CHAPTER 3 : Shape Synthesis of a MIMO DRA

3.1 Introduction

Based on the investigation of lower bounds of DRA substructure and a novel shape synthesis method[64], this chapter introduces a design process of a MIMO DRA with a complex shape. The chapter's main objective is to provide guidance on the design flow of the MIMO DRA for researchers. Since fewer DRAs of non-canonical geometries are introduced than conventional shapes, the design of the structure and feed network is illustrated in detail. Simulation results are compared before and after each step to explain how changing the design affect the performance. Even though one case study of a MIMO DRA is addressed in the chapter, it can be applied to design the other MIMO DRAs with different specifications.

The optimization process for DRAs has similar steps to the shape synthesis procedure described in [65], for metallic antennas. Figure 3.1 represents the overall concept of the design procedure. First, the geometry of the DRA superstructure is selected based on the design requirements and a sub-structure is synthesized by the optimization code based on CMA and binary genetic algorithm (GA). Then the DRA is fed by a decoupling technique [4] to improve the antenna’s reflection coefficients and mutual coupling. At last, the designed DRA is fabricated by 3D printing technique. In this paper, since the practical fabrication is limited due to COVID-19, a preparation process for the fabrication and an available 3D printing technology are introduced.

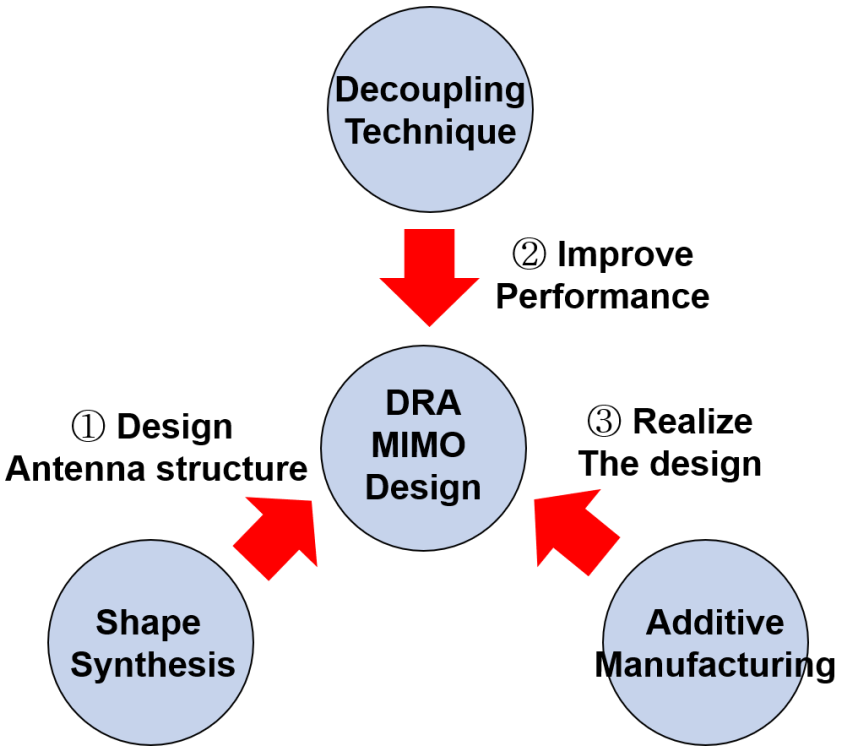

Figure3.1: Design procedure of MIMO DRA

3.2 Antenna Shape Synthesis

The shape synthesis method for an optimized DRA follows a related procedure described in the recent papers for planar microstrip antennas [64, 65]. The first step is deciding the proper dimension of the antenna's superstructure. The investigation of lower bounds of the DRA substructure described in the previous chapter is applied in this step. If we excite 'k' numbers of characteristic modes with a single dielectric resonator at a certain frequency, at least 'k' of characteristic modes of its superstructure should resonate below that frequency before the optimization. Because the resonance of characteristic mode moves to higher frequencies during the optimization since we remove some parts from the super structure to excite 'k' modes at one frequency. Thus, we can shift the resonance of each mode by different amount of frequency and excite them at one frequency by the shape synthesis method.

Then the superstructure is optimized by the code based on binary GA and CMA. As done in chapter 2, the optimization code removes unnecessary parts(tetrahedra) from the structure based on the cost function. The presence and absence of each tetrahedron are represented as the binary gene in the code and the cost function varies with which parameter is weighted in designing MIMO DRA. As a result of the code, the best DRA substructure for the cost function is obtained by the optimization process of the genetic algorithm in Figure 2.1. The details are coved in the following section with a case study.

Next, the optimized structure is analyzed and the eigencurrent plots of the structure are obtained by CMT. The eigencurrent plot of each characteristic mode shows how the current flows in the structure and we place the feed at the point where the eigencurrent flows strongest. The placed feed excites a similar current and mode with the observed mode in eigencurrent plot, however, the excited mode will be a combination of characteristic modes. It is not practically easy to place the feed exactly at the strongest point and to excite the desired mode only. Therefore, we use a matching and decoupling technique to improve the antenna's performance as shown in step 2 of Figure 3.1. Since the optimized structure has arbitrary shape, we have flexibility in this step and diverse techniques can be used. This paper covers coaxial probes and slot feeding.

The step 3 is fabricating the DRA by 3D printing technique. Before that, there is a preparation step for the fabrication. Weak connections in the structure are manually reinforced and sharp parts are filleted to prevent breaking. A hole is drilled into the antenna structure if it is fed by a coaxial probe. Ideal parts of design such as a perfect ground plane, perfect conductor are replaced by the practically available one. Since some of these process affect the antenna's performance, additional matching process is required. After the preparation step, the antenna structure is printed and then we can measure the design in practice.

3.3 Step 1 - Shape Synthesis of three ports MIMO DRA

In this section, the shape synthesis method described above is applied to a certain case. First, here we assume that $25 \times 40 \times 16mm^3$ of space are available for the DRA design and DRA structure is composed of high permittivity material, Zirconia($\varepsilon_r = 23$). Based on the assumptions, we design a 3 port MIMO DRA in this section since not many research papers have tried to excite three different modes with a complex-shaped DRA. First, the available space is considered as a geometry of DRA superstructure and we will synthesize the MIMO DRA structure by removing parts from the super structure.

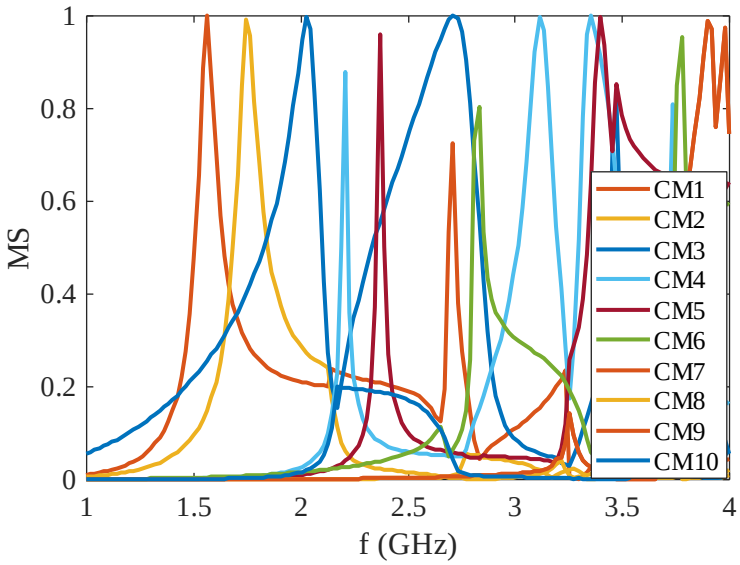

Figure 3.2: Characteristic modes of DRA superstructure

Figure 3.2 is the CM analyzed result of the DRA superstructure and 10 characteristic modes are represented. As investigated in the last chapter, the desired operating frequency of MIMO DRA should be higher than the third resonance of the DRA superstructure. Figure 3.2 shows the first three modes resonate at 1.55GHz, 1.75GHz and 2.02GHz. According to the lower bound of the resonant frequency discussed in the prior chapter, the lowest possible frequency for 3 port DRA is principally around 2.02GHz. However, as the volume of the structure is reduced in the

optimization process, the frequency of third mode is expected to be higher than 2.02GHz in practice. Therefore, MIMO DRA's operating frequency is determined to be 2.45GHz in consideration of Wifi communication.

Then, as a step 1 of Figure 3.1, the structure is optimized by the GA and CMA-based code. The code synthesizes the rectangular structure to resonate three different modes at 2.45GHz with the following cost function[65] :

$$\text{Cost} = \sum_{n=1}^{3} C_n + a_2 V \quad (1)$$

Where $C_n = a_1(1 - MS_n) + Q_n$ means contribution of each mode and a_1 represents the weighting coefficient between the resonant frequency and the Q factor of the mode. V is the volume of the substructure normalized to the volume of the superstructure, and the role of V in the cost function is removing unnecessary tetrahedra during the optimization. In this paper, $a_1 = 200$ and $a_2 = 10$ are used to put high weight in the order of modal significance, reducing volume and Q-factor. These coefficients and cost function represent that the optimization code focuses on resonating three modes at 2.45GHz. Regarding the optimizing calculation, two conditions are assumed. Symmetry is forced in x and y dimensions to simplify the geometry and expedite the optimization [64]. For this initial optimization step, an infinite ground plane is considered and loss is ignored.

Figure 3.3 is the side view and isometric view of the optimized structure, that is conducted by Dr.Yang. Some tetrahedra are removed from the superstructure under the cost function. Figure 3.4 (a) is the comparison of the modal significance result between the complete structure and the optimized structure. Before the optimization, the resonant frequencies of mode 1, 2 and 3 were 1.57GHz, 1.75GHz and 2.05GHz respectively. Each resonant frequency moves to 2.43GHz, 2.43GHz and 2.59GHz after the optimization. There is small deviation in the resonant frequencies

of three modes, but the result is much better than the superstructure's result and it can be improved by a feeding technique.

Figure 3.4 (b) shows that the modes of the optimized structure have lower Q factor than that of superstructure. Q-factor of each mode was 440, 13, 38 before the optimization and they reduce to 14, 17 and 8 after the optimization. In relation to the lower bound of Q factor in the last chapter, the results show that Q factor of DRA substructure can be lower than the value of superstructure above the first resonant frequency.

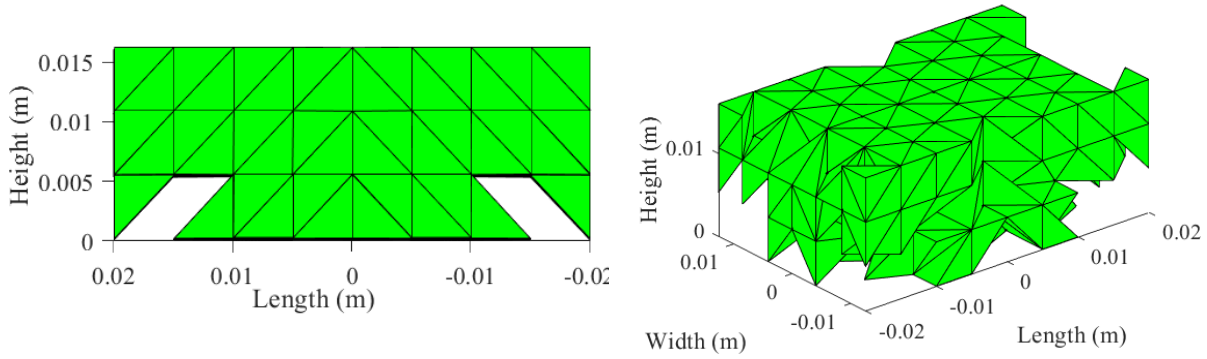

(a) a side view (b) an isometric view

Figure 3.3: The optimized structure for DRA MIMO

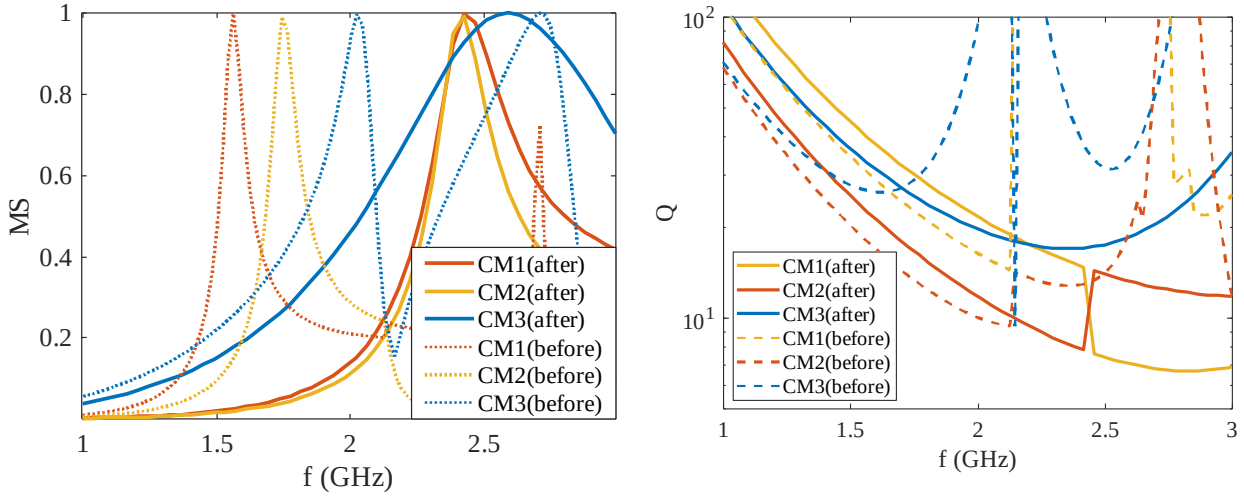

(a) MS results (b) Q factor results

Figure 3.4: Comparison Modal significance results before and after the optimization

Figure 3.5 represents the eigencurrent results of each resonant mode obtained by CMA. It shows total current and highlights the tetrahedra in red where the eigencurrent flows strongly. And the blue region represents where the eigen current flows weakly. Eigencurrent in mode 1 flows from the end to the other end of the structure's longest dimension and current in mode 2 flows in W(shortest) dimension. Mode 3 has the highest current point at the center of the structure and the current flows to the edges along to the longest(L) dimension of the structure. Based on this, feeding positions are roughly decided; at the center, on the x-axis, on the y-axis. Since feeding at any point excites a combination of characteristic modes, we will move the feeding position and find the best position by observing a smith chart in the next section. Then the antenna performance is improved by matching and decoupling techniques

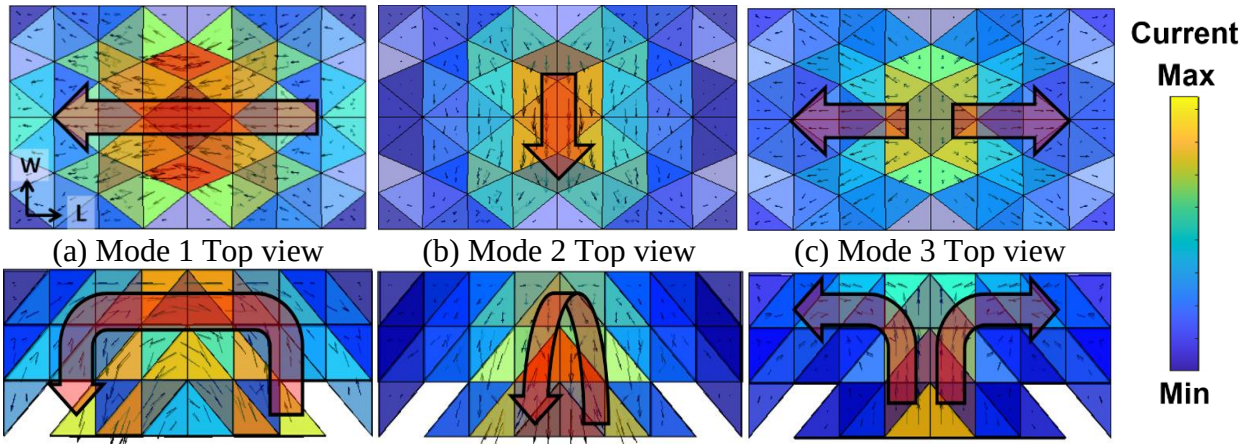

(a) Mode 1 Top view (b) Mode 2 Top view (c) Mode 3 Top view

(d) Mode 1 Side view (e) Mode 2 Side view (f) Mode 3 Side view (g) Scale

Figure 3.5: Eigencurrent(polarization current) of resonant modes

3.4 Feeding Technique

3.4.1 Three coaxial Probes

According to the expectation from the Figure 3.5 result, three coaxial probes are initially implemented at the bottom of the structure as shown in Figure 3.6. It is expected that coupling and

reflection coefficient can be adjusted by changing the height, radius and location of coaxial probes[10].

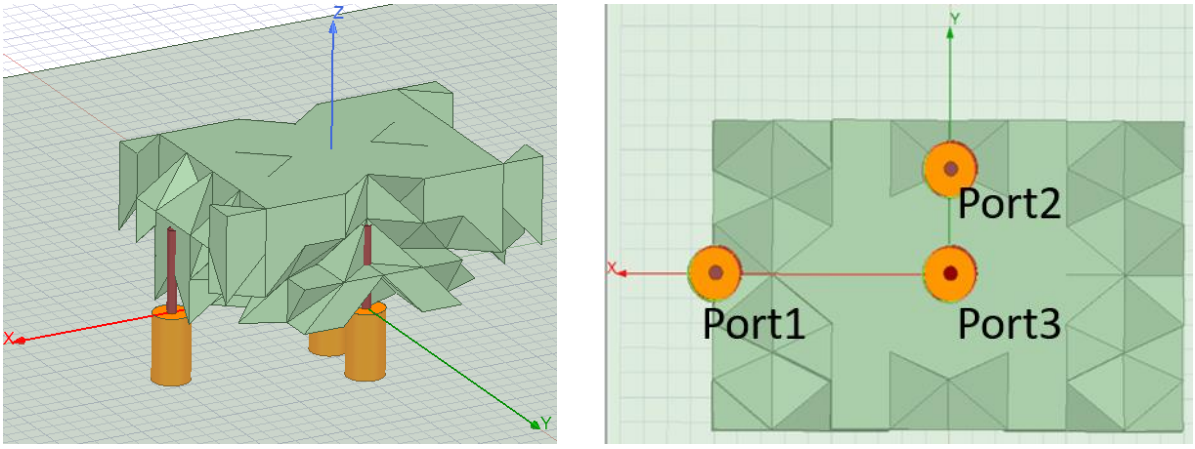

(a) isometric view (b) bottom view

Figure 3.6: Feeding with three coaxial probes

Port 1 is located along the x-axis and excites the mode 1 in Figure 3.5. By moving its position, we found the probe should be located between (15mm,0,0) to (20mm,0,0) to excite the mode since the real impedance becomes lower than 1Ω as the probe is closer than 15mm from the origin point. To have the maximum value of the real impedance, port 1 is located at (20mm,0,0)

Figure 3.7 shows smith charts with the range of 2.4GHz to 2.5GHz with changing radius and height of the probe. (a) shows the real part of impedance decreases and the imaginary part increases as the radius of the probe increases. (b) shows the height of the probe is proportional to both real and imaginary parts of impedance at 2.45GHz. However, the real impedance at 2.45GHz did not reach 50Ω with the height and radius range of 7mm~16mm and 0.1mm~1mm.

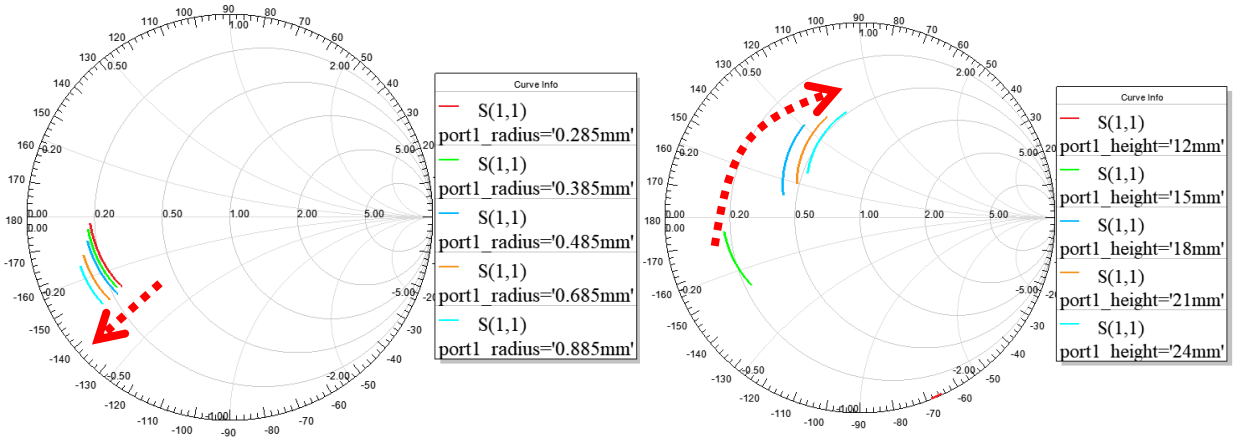

(a) Change Radius of Probe (b) Change Height of Probe

Figure 3.7: Smith chart results of coaxial probe feeding(Port1)

Port 2 is located on the y-axis and excites the mode 2 in Figure 3.5. Regarding the location, the real impedance increases as the probe moves from (0,12mm,0) to (0,7mm,0) and then decreases. The maximum value of the real impedance was 20 Ω. Detailed data for Port 2 are not shown here because changing the radius and the height of the port affects the impedance in the same way as port 1. Port 2 also has difficulty in increasing the real impedance at 2.45GHz.

Port 3 should be located at the origin point to excite mode 3 due to its symmetrical shape. Figure 3.8 shows smith chart results with changing radius and height of the probe. Fig. 3.8(a) shows the radius of the port is reversely proportional to both real and imaginary parts of impedance. On the other hand, the probe height tends to cause rotation on the Smith chart as shown in Fig. 3.8(b). Compared with port 1 and 2, tuning two parameters of probe 3 increases the real impedance more, therefore, it can be matched at 2.45GHz.

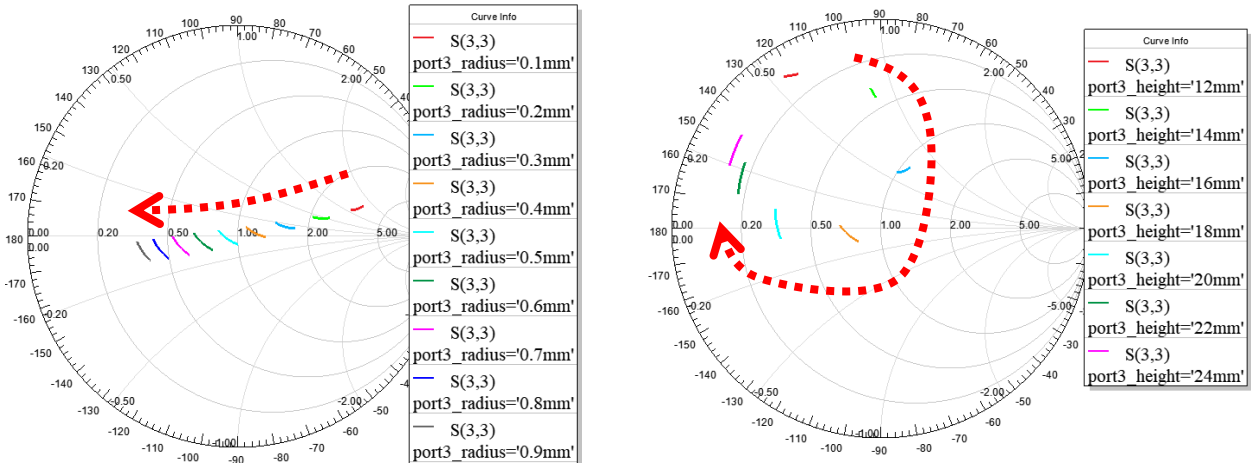

(a) Change Radius of Probe (b) Change Height of Probe

Figure 3.8: Smith chart results of coaxial probe feeding(port3)

Figure 3.9 shows the S-parameter result after matching the ports. Each port resonates at 2.3GHz, 2.3GHz and 2.4GHz. The resonant frequency of ports 1 and 2 cannot be higher than 2.3GHz with the matching process, on the other hand, port 3 has more flexibility in the resonant frequency, from 2.1GHz to 2.6GHz. Couplings at 2.45GHz are -8dB to -20dB, which are not affected by changing the probes' radius and height. The final parameters of each port are shown in Table 3.1.

Table 3.1 : Coaxial Probe Specification

	Exciting mode	Radius	Height	Position
Port 1	Mode 1	0.3mm	16mm	(18mm,0,0)
Port 2	Mode 2	0.385mm	8mm	(0,8.45mm,0)
Port 3	Mode 3	0.45mm	10mm	(0,0,0)

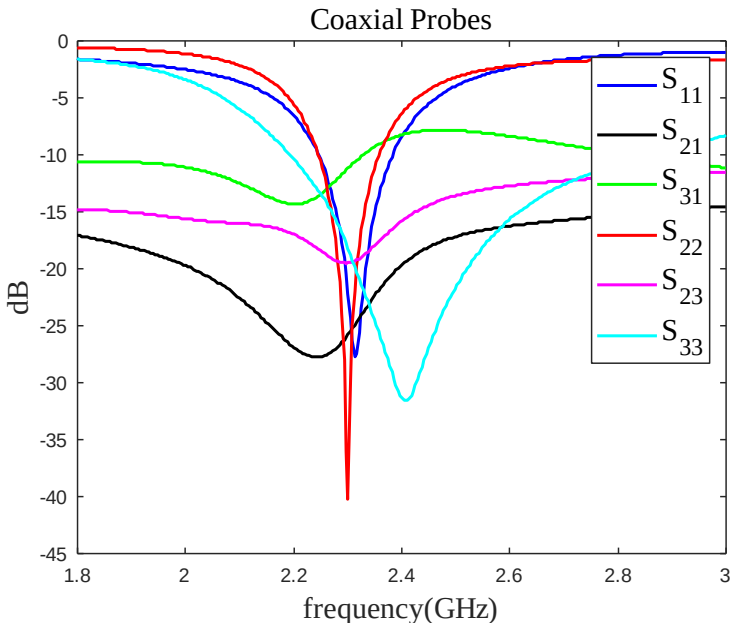

Figure 3.9: S-parameter result of Coaxial probe feeding

3.4.2 Decoupled mode with Probe and Slots

Coaxial probes have a limitation in increasing the real impedance for all three ports and the high couplings at 2.45GHz, especially between ports 1 and 3. Due to these limitations, coaxial probes of ports 1 and 2 are replaced by slots as a matching and decoupling technique [4] and one coaxial probe at the origin point remains the same. Figure 3.10 introduces the concept of the technique by showing magnetic fields of ports. (a) shows magnetic fields of three coaxial probes and (b) shows magnetic fields after changing two coaxial probes to slots. Comparing with the three coaxial probes, the directions of the magnetic fields from the ports are more perpendicular to each other, yielding better coupling values.

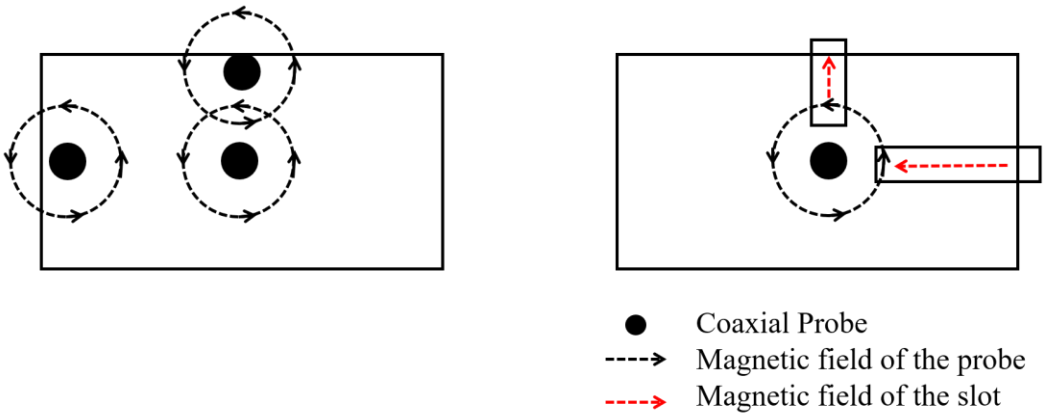

(a) Three coaxial probes (b) Coaxial probe and slots

Figure 3.10: Magnetic fields of the feeding network

To investigate the decoupling technique by simulation result, each coaxial probe of ports 1 and 2 is firstly replaced with a single slot as shown in Figure 3.11. The microstrip lines are located at the center of slots and have 2mm of width, calculated to be 50Ω by using a microstrip line calculator[66]. Slot sizes of ports 1and 2 are $3 \times 16mm$ and $3 \times 11mm$. The coaxial probe for port 3 remains the same. Figure 3.11 (b) shows the sideview of the design by stacking up the layers. The DRA structure is mounted on the PEC ground plane. The material of substrate is a modified epoxy with 4.2 of permittivity and 1mm of thickness.

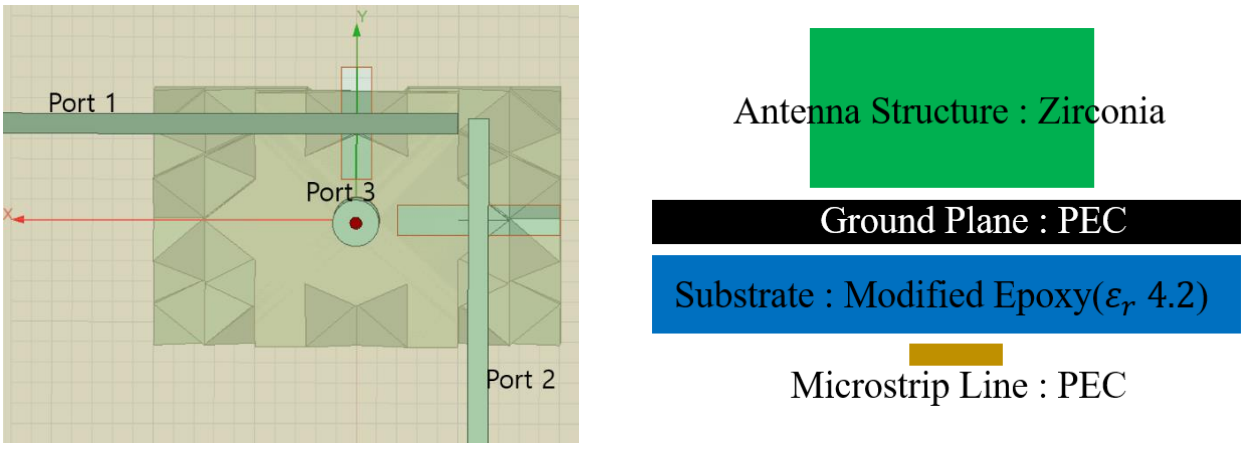

(a) Bottom view of the design (b) Side view (Stack up)

Figure 3.11: Feeding with two slots and one coaxial probe

Coupling results of three coaxial probes and one probe with two slots are compared in Figure 3.12. Overall coupling results are improved after two probes are replaced by slots. Couplings between port 3(probe) and slots, S_{13} and S_{23}, are less than -40dB while S_{21} is still higher than -22dB at 2.45GHz.

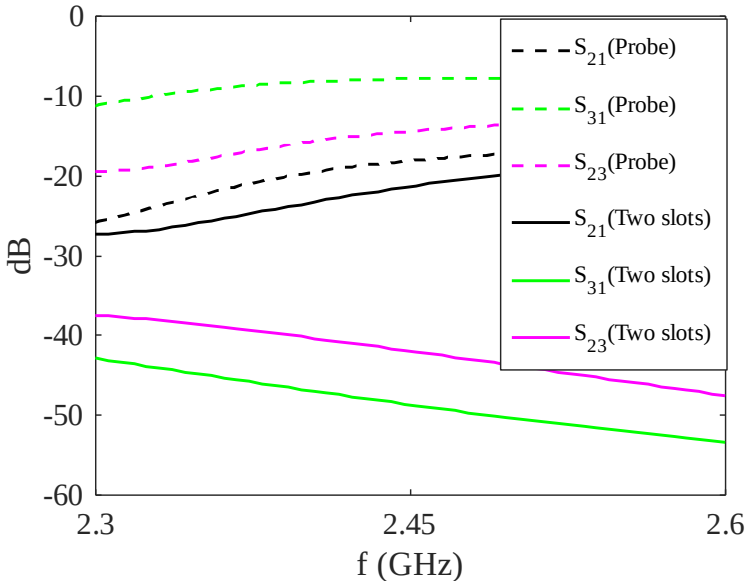

Figure 3.12: Coupling results of three coaxial probes and one probe with two slots

Then an additional slot is implemented on port 1 as shown in Figure 3.13 in order to reduce S_{21} by referring [4]. The research paper used two pairs of balanced slots with one coaxial probe, however, we use the balanced slots only for port 1 to avoid complicating the design. (a) and (b) show the bottom and isometric views of the design. Port 1 has two symmetrical slots with a T-junction. Port 2 and 3 are the same with Figure 3.11 (a).

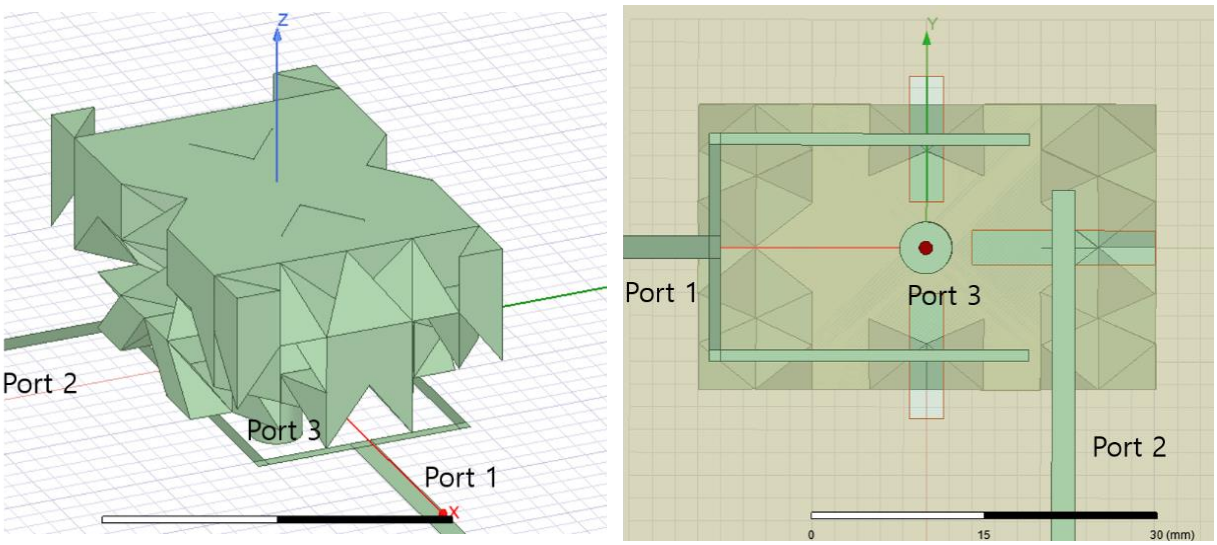

(a) isometric view (b) bottom view

Figure 3.13: Feeding with a coaxial probe and three slots (decoupling network)

Figure 3.14 is the initial S-parameter result of the design. Including S_{21}, all ports have much lower coupling values(<-40dB) than previous feeding techniques. S_{23} over frequency range decreases from -40dB to -50dB and S_{21} decreases from -25dB to -40dB. On the other hand, all ports have poor reflection coefficients since each port has 8Ω, 13Ω and 39 Ω of real impedance values at 2.45GHz.

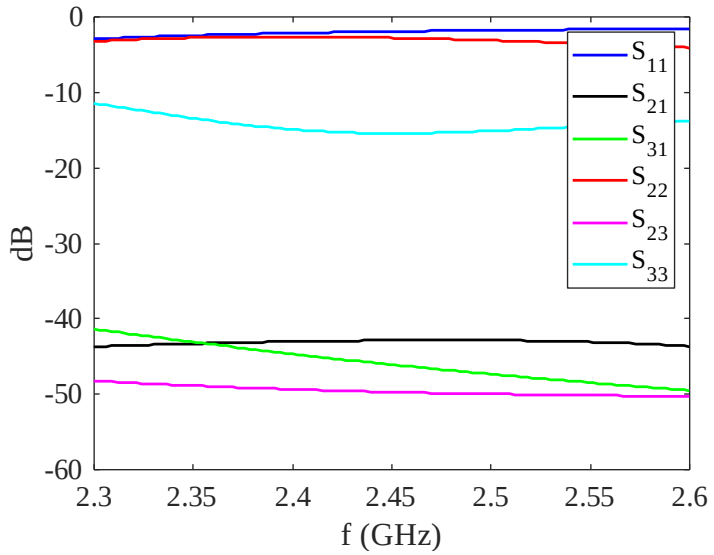

Figure 3.14: Initial S-parameter result with decoupling network

As the next step, the reflection coefficients of the ports are improved by stub matching. Since the matching technique for port 3 is already covered in the previous section and that port 1 and 2 barely affect port 3, only port 1 and 2 are addressed in this section.

Regarding the port 1 matching, the key variables affecting the reflection coefficient were the position and length of the stub. Smith charts are mainly used for the analysis by examining the impedance under the microstrip line's T-junction. Figure 3.15 (a) shows the Smith chart result as the stub moves outward from the T-junction of the microstrip line to the port by 5mm steps. (b) shows that the stub length is proportional to the imaginary part of impedance, while the real part is not affected.Port 2 is matched in the same way with port 1. The stub position and the length change with parametric sweep and S-parameter results were observed.

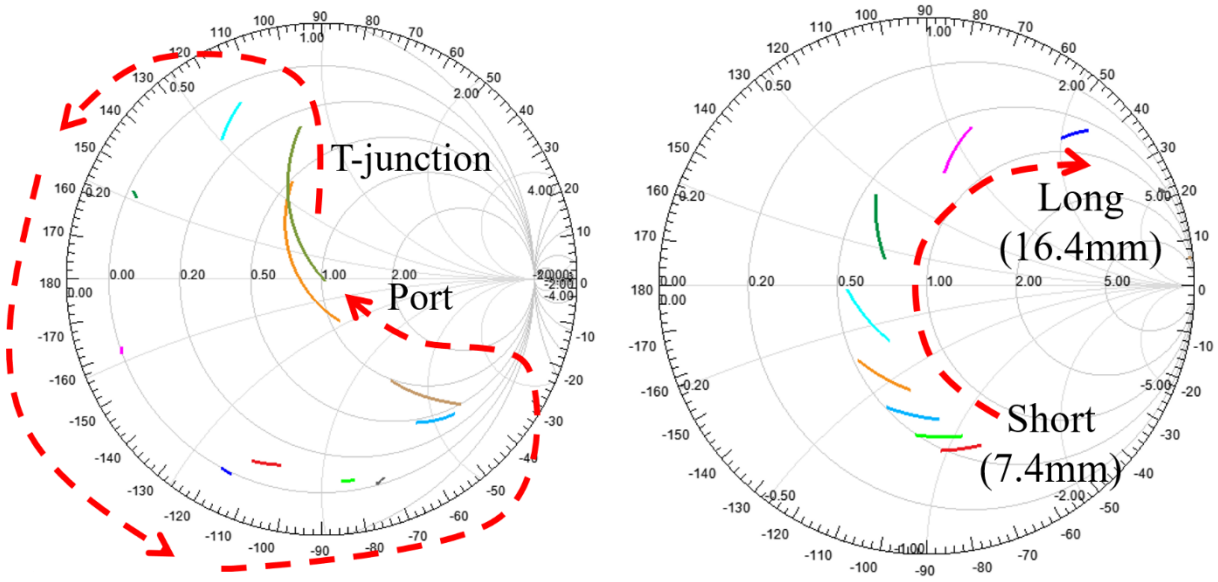

(a) Stub position (b) Stub length

Figure 3.15: Smith chart result with changing stub position and length

Figure 3.16 is the S-parameter result of the design. Comparing with the result of three coaxial probes, both coupling and matching results are improved significantly. All three modes

resonate at 2.45GHz with -35dB of reflection coefficients and the coupling results are also less than -30dB. One possible disadvantage of using slots is a more complex and larger feeding network due to the additional microstrip substrate and transmission lines.

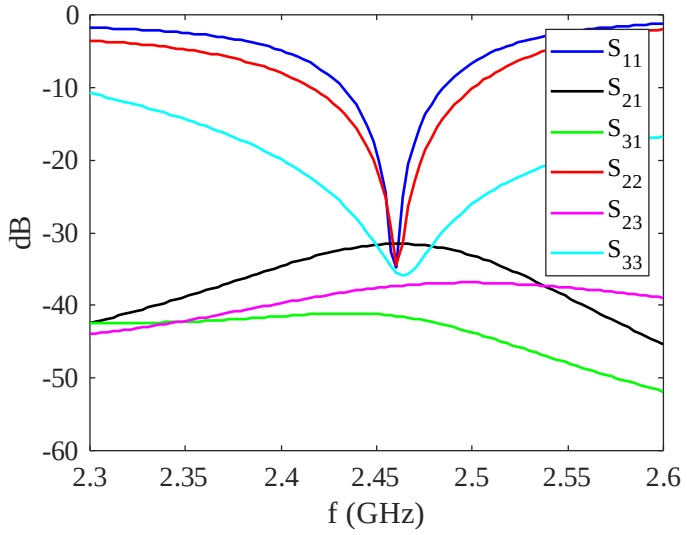

Figure 3.16: S-parameter result with decoupling network

3.5 Fabrication Procedure

The fabrication procedure of the designed MIMO DRA is covered in this section. Since the high dielectric constant material is used for the designed antenna structure, the traditional milling method is not well-suited to fabricate it due to the cost and ability to create intricate shapes. On the other hand, the advanced 3D printing technique provides low cost, time-efficiency and high precision in shaping the high dielectric constant material. However, due to COVID-19, we were unable to print and measure DRA during the timeframe of this thesis. Therefore, this section provides the preparation procedure for the practical 3D printing and the final simulation results. Also, the available manufacturing method and some expected limitations are covered at the end.

3.5.1 Preparing Antenna for Fabrication

In the optimized antenna structure in Figure 3.3, some parts are hard to realize in practice and need to be improved for the fabrication. First, the red circles in Figure 3.17 show eight small parts of the antenna structure meet the main body with only a single edge and have week connections. To improve the connection, 1mm-thick bridges are built along the linking edges between the parts and the main body. Second, sharp edges and vertices of the structure are filleted to curved faces with a 0.5mm radius since these parts are vulnerable to shock and easy to break. 3D CAD modeling software, Solidworks and Spaceclaim, are used in this preparation step.

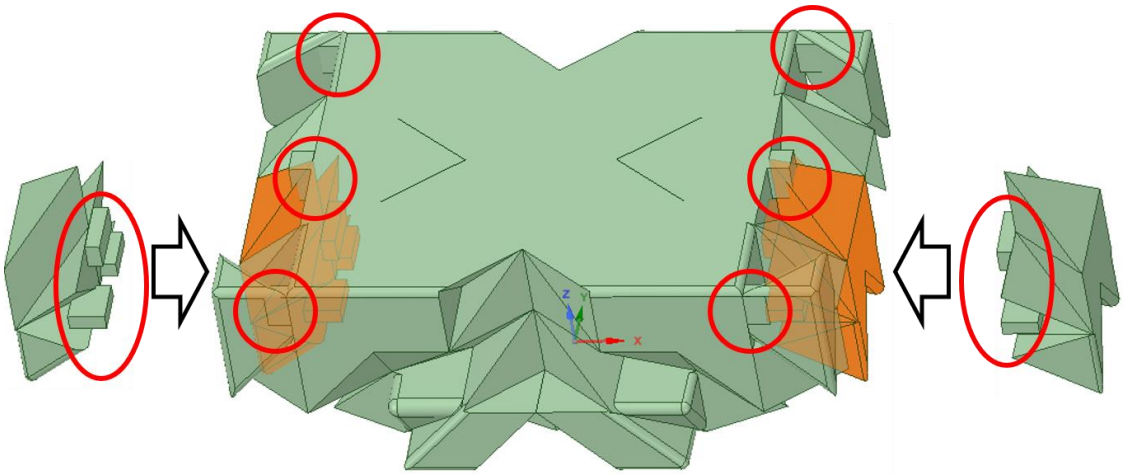

Figure 3.17: Preparing antenna structure for the fabrication

Figure 3.18 shows the S-parameter results before and after the preparation step. Overall, there is no significant difference. The port3(coaxial probe) result decreases 3dB while S_{11} and S_{22} performs slightly better. Couplings between each port are almost the same. Since all values in both plots are still lower than -30dB and the differences are smaller than 1%, the preparation step can be assumed not to affect the S-parameter result.

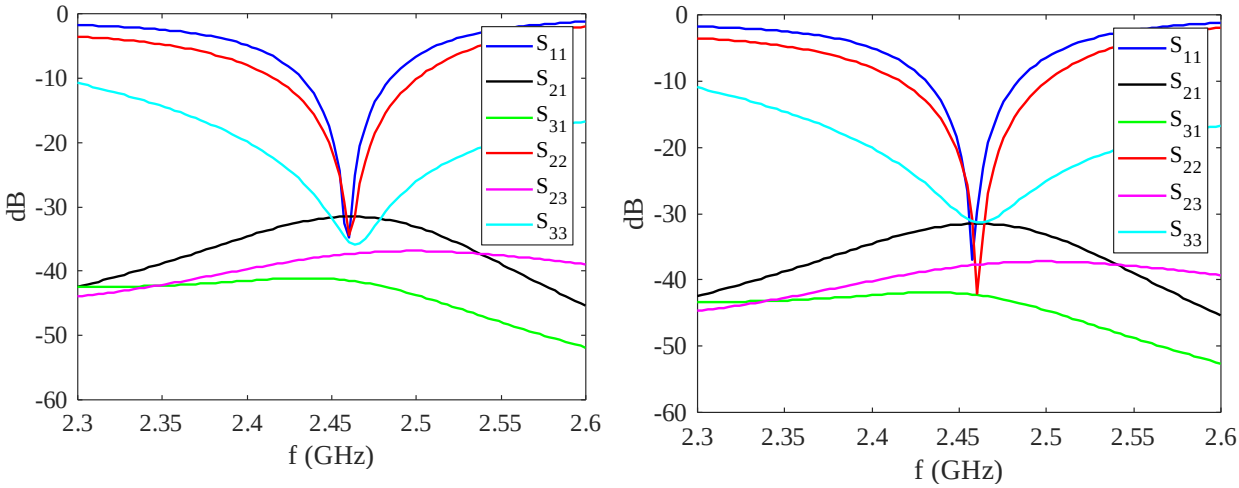

(a) before (b) after

Figure 3.18: S-parameter results before and after changing the structure

3.5.2 Airgap Sensitivity in Using Probe Feed

In the fabrication process, it is necessary to create a hole to put the probe into the antenna body, which should be slightly larger than the probe. Fabrication limitations makes it likely that there will be some space between the probe and antenna structure, called airgap in this paper. Figure 3.19 shows a schematic of the airgap, the probe and the hole. This part addresses the sensitivity of the S-parameter results to the airgap. The assumption is both the hole and probe are perpendicular to the ground and the airgap size around the probe is constant so the probe does not touch the antenna body.

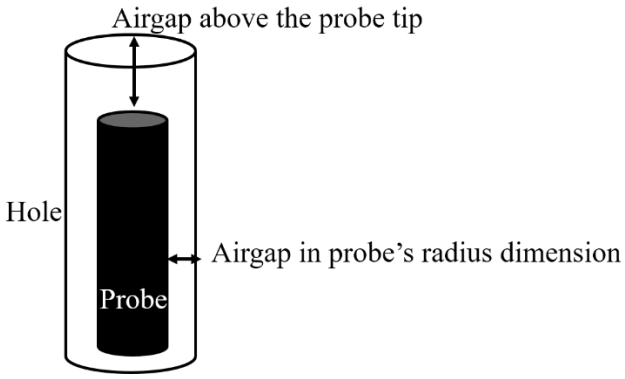

Figure 3.19: Airgap Schematic

To investigate the sensitivity of the air gap, we conducted simulations with different radius of probe and airgap. Figure 3.20 presents the reflection coefficient result of two cases. 0.585mm and 1mm are used for the probe radius in (a) and (b). When the probe radius is 0.585mm, S33 result keeps below -20dB until the air gap is 0.005mm and increases quickly after then. On the other hand, with 1mm of probe radius in (b), the reflection coefficient was less than -20dB until the airgap size reaches 0.02mm, which is larger than the former case. Based on these two cases and some additional simulations, we found that the acceptable airgap size is proportional to the probe's radius.

However, recalling the Smith chart result in Figure 3.7, another consideration is the probe radius at port 3 is inversely proportional to the impedance. At 2.45GHz, 0.585mm and 1mm of radius have 54Ω and 24 Ω of real impedances. Based on two considerations and simulation results, 0.635mm of probe radius and 0.01mm of the air gap is used in the final simulation. The airgap above the probe tip barely affects both reflection coefficient and coupling result, so 10mm of height is maintained with 1mm air gap above the tip.

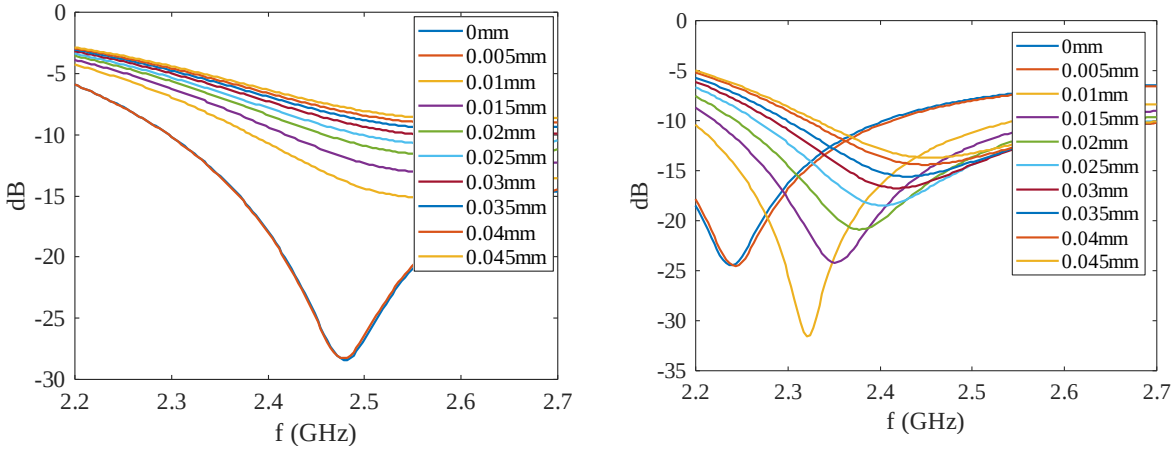

(a) 0.585mm of probe radius (a) 1mm of probe radius

Figure 3.20: Sensitivity of reflection coefficient due to airgap.

3.5.3 Final simulation result

Microstrip line, substrate and the probe also changed from the ideal one to practically available one. Instead of the perfect ground plane, Duroid 5880 is used for the substrate with 0.79mm of thickness, 0.0004 of loss and 2.2 of permittivity. Zirconia with 23 of permittivity and 0.0013 of loss tangent is used for the DRA structure. The perfect conductor of the ground plane changed into copper with 0.01mm of thickness. SF2950-6200 from Amphenol is used for the SMA connector and four holes are drilled into the substrate to connect the coaxial outer conductor to the DRA ground plane with thin copper cables. Simulations show that the grounding vias do not affect the result. On the other hand, changing substrate affects the matching result, therefore, the microstrip line width, stub position and length are tuned again. The revised microstrip lines are 2.4mm wide and all slots are $3 \times 14mm^2$. Based on the behavior in Smith chart of Fig. 3.15, the length and position of stubs are tuned to improve the match of each port.

Figure 3.21 is the S-parameter and envelope correlation coefficient(ECC) results of the final design. S-parameter result shows the reflection coefficients are less than -22dB and couplings are also better than -37dB at 2.45GHz. ECC represent how independent each radiation pattern is. In the ECC plot, all coefficients have nearly zero at the target frequency, meaning the radiation patterns of the ports are almost completely independent. ECC is defined as following [67] :

$$\rho_{mn} = \frac{\left|S_{mm}^{*}S_{mn} + S_{nm}^{*}S_{nn}\right|^2}{(1 - \left|S_{mm}\right|^2 - \left|S_{nm}\right|^2)(1 - \left|S_{nn}\right|^2 - \left|S_{mn}\right|^2)} \tag{17}$$

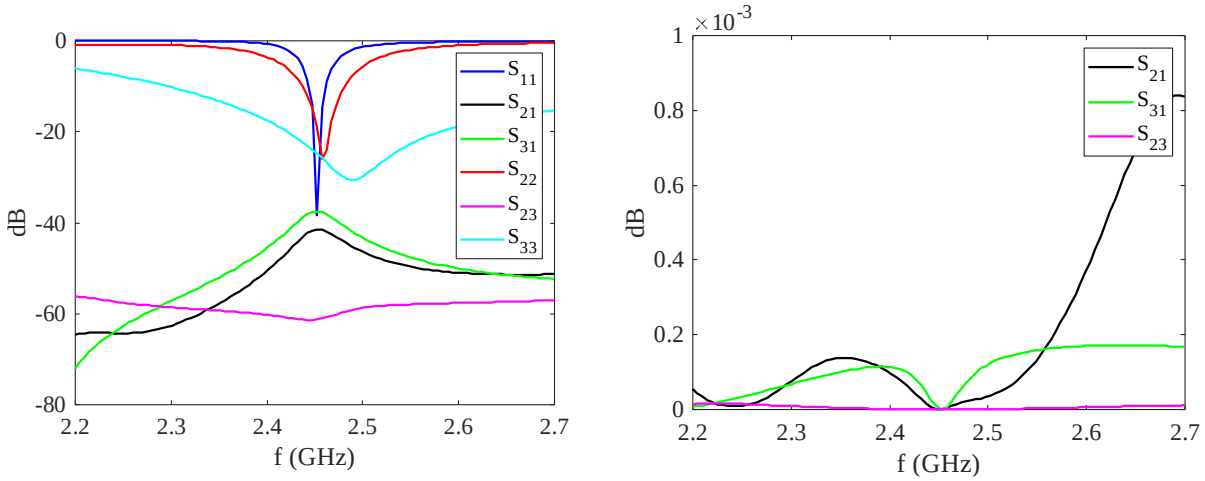

(a) S-parameter result (b) ECC result

Figure 3.21: S-parameter result of the final design

Figure 3.22 shows the simulated radiation patterns of each port at 2.45GHz. (a), (c) and (e) show co-polarization and cross-polarization of port 1, port 2 and port 3 on the E plane. Red and black lines respectively represent E_θ and E_ϕ fields. Figure (b), (d) shows these on H-plane. (e) shows these polarizations on $\theta = 45°$, where port 3 has the highest directivity. Port 1 and 2 have broadside radiation patterns on both E and H planes. Peak gains of ports 1 and 2 are 6.53dB and 6.36dB. At $\theta = 0°$, co-polarized fields in (a)~(d) are stronger than cross-polarized fields by around 40dB. Due to the ground plane effect, in Figure 3.22 (e), the radiation pattern of port 3 on x-z plane is tilted and has 3.47dB of the peak value at $\theta = 45°$. (f) is radiation pattern of port 3 on x-y plane and shows the port 3 radiates omnidirectionally.

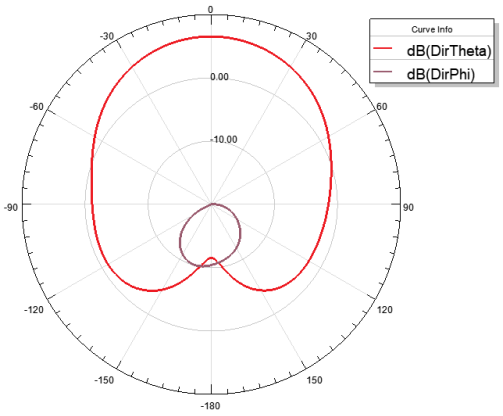

(a) Port 1 E plane(x-z plane)

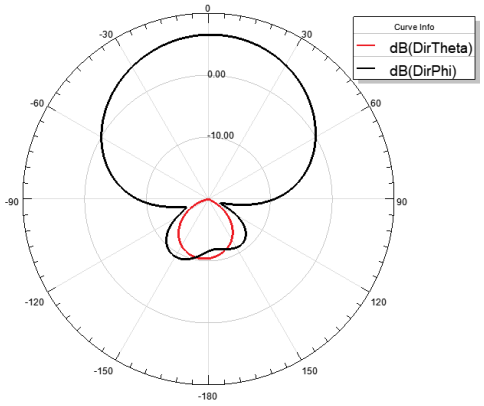

(b) Port 1 H plane(y-z plane)

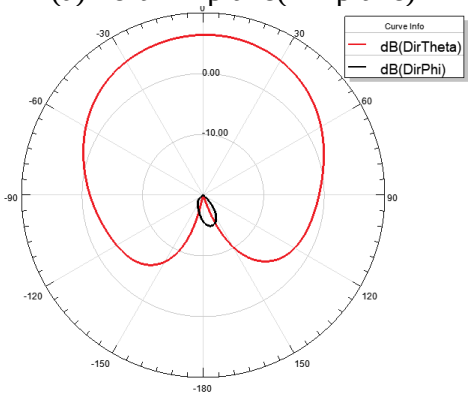

(c) Port 2 E plane(y-z plane)

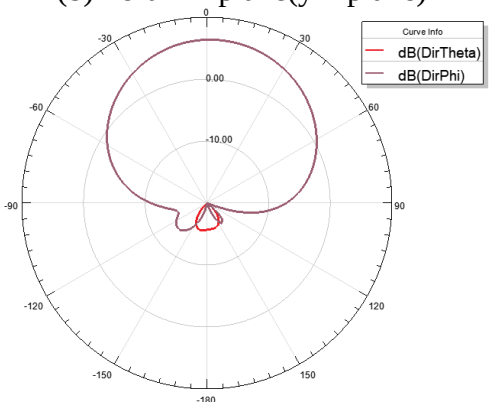

(d) Port 2 H plane(x-z plane)

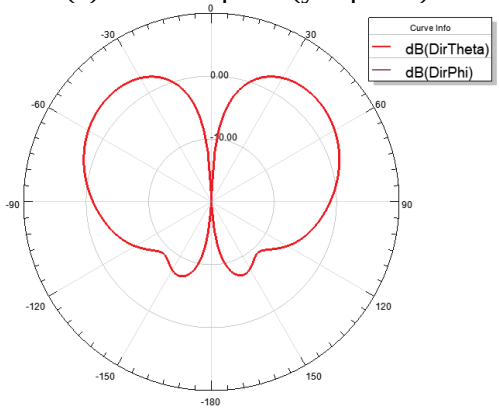

(e) Port 3 x-z plane

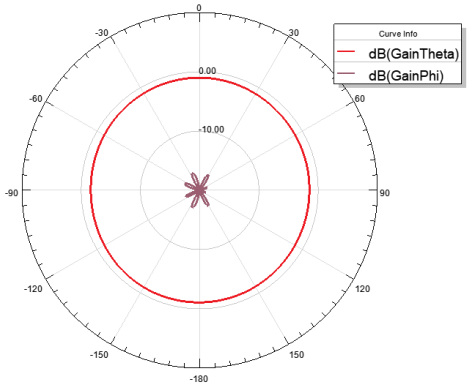

(f) Port 3 x-y plane

Figure 3.22: Radiation patterns of ports

3.5.4 Available 3D Printing Technique.

Regarding the printing method, it should be carefully selected depending on the research purpose, design complexity and permittivity. In our case, since the permittivity is high(ϵ_r =23) and the structure design also has an arbitrary shape, the printing technology is required to high

printing resolution for that material. Few options are available for printing ceramic materials with high permittivity, but the plan for the present work is to use NanoParticle Jetting technology from XJet [50]. This technology uses a lot of tiny print-heads, each containing 512 nozzles. As a method, these print heads deposit fine droplets onto a heated build plate. The droplets consist of carrier-liquid, support material and build material and carrier-liquid is completely evaporated after deposited by heat. Then remaining build materials are bond to each other and a roller travels over the printed layer to flatten the layer precisely. With the technology, zirconia structure can be printed with $10\mu m$ of layer thickness and $20\mu m$ of the resolution, which is small enough and might not affect the result. Based on recent results with this printer [50,68], we expect to be able to obtain a highly accurate zirconia structure with this method.

3.6 Discussion

This chapter provided a design procedure of MIMO DRA with a non-canonical shape. As a case study, the rectangular superstructure and permittivity of 23 are used to design MIMO DRA operating at 2.45GHz. Even though the design procedure has flexibility depending on the desired antenna specification, the overall procedure will apply to different structures and dielectric constants.

Regarding the feeding technique, the balance slots for port 1 had a better decoupling result than using a single slot. We can apply it to the coaxial probe feeding in the future. Recalling the coaxial probes had limitations of the high coupling and low real impedance, using a pair of (balanced) probes for the ports could address the high coupling result. If two limitations of the coaxial probe feeding are efficiently addressed with the balanced port and one more technique, that also could be a good feeding technique. Besides, that feeding technique could have an advantage in terms of the antenna's overall dimension.

One limitation is that the antenna is not fabricated in practice. According to [50], there is uncertainty about the exact dielectric constant and loss tangent of the printed structure. It varies with the material, frequency and height of the printed structure. Based on the results in that paper, each permittivity and loss tangent will have deviations of 23 ± 1 and $(1.3 \pm 0.6) \times 10^3$at least. Therefore, we cannot guarantee that the printed structure and the measured result will be the same with the simulation result.

3.7 Summary

Based on analyzing a rectangular DRA, the resonant frequencies of characteristic modes are calculated and the target resonant frequency(2.45GHz) is chosen above third resonance. The DRA structure is optimized by in-house code to excite three different modes at 2.45GHz and feeding positions are roughly chosen by eigen current plots. The feeding with three coaxial probes has limitations in coupling and matching, therefore, two coaxial probes are replaced by slots. One port has a single slot and the other port uses a pair of slots with a Wilkinson divider. This feeding technique showed better mutual coupling results. Stubs are used to improve the reflection coefficient of two ports.

Then some ideal parts are tuned manually before fabrication and the results before and after the process are compared. Sharp parts in the structure are filleted and eight bridges are added in weak-connected parts. And a hole for the coaxial probe is drilled into the antenna structure with an air gap between the antenna body and probe. Filleting the edges and adding bridges did not affect the result, on the other hand, the air gap size sensitively influences the reflection coefficient of the coaxial probe.

The overall performance of the antenna is quite good. Table 3.2 compares the design to the existing 3-ports MIMO DRAs. The design uses a higher permittivity and has a mid-size in wavelength scale. It has better reflection coefficients and coupling results, however, one drawback of the design is narrower fractional bandwidth than other DRAs.

Table 3.2: Comparison to the existing DRAs

	Antenna shape / size (wavelength in material)	Operating frequency (Wave length in material)	Dielectric constant	Reflection Coefficient	coupling	Fractional Bandwidth
[4]	Cylindrical Radius: 0.67λ Height : 0.8λ	2.45GHz (39.11mm)	9.8	<-22dB	<-24dB	100MHz
[38]	Rectangular $3.2\lambda \times 1.77\lambda \times 1.34\lambda$	9.48GHz (9.9mm)	10.2	-10~-30dB	<-20dB	720MHz
[39]	Rectangular $1.16\lambda \times 1.16\lambda \times 0.9\lambda$	2.45GHz (26.72mm)	21	-10~-20dB	-11~-15dB	100MHz
Design	Complex $0.97\lambda \times 1.56\lambda \times 0.62\lambda$	2.45GHz (25.53mm)	23	<-22dB	<-37dB	15MHz

CHAPTER 4: Conclusion and Future Direction

4.1 Summary of Thesis

In chapter 2, the lower bounds of Q-factor and the resonant frequency on DRA substructures are represented below the first resonance of DRA. A recent paper[9] proved the capacitive nature of DRA and the lower bounds mathematically, and numerical examples support it in this chapter. The examples showed how the antenna shape, resonant frequency and Q factor of DRA changed as the MoM-based code optimized the antenna structure to have lower values. The results showed that Q-factor and resonant frequency decreased over generations of the optimization, however, they cannot break the lower bounds of the complete structure. Also, the shapes of substructures gradually changed and ended up being the complete structure after optimizations.

Chapter 3 introduces the novel design methodology of MIMO DRA, including shape synthesis and decoupled feeding technique. The dimension of the superstructure was selected to have its first three self resonances lower than 2.45GHz. Then the structure was optimized to resonate the three modes at 2.45GHz and its eigencurrent plots provided approximate feeding locations. Two types of feeding techniques were simulated: three coaxial probes and the combination of slots and the coaxial probe. Using three coaxial probes has limitations of high coupling and low impedance at 2.45GHz. On the other hand, after two coaxial probes are replaced with slots, the MIMO DRA showed a better decoupling and matching performance than three coaxial probes. In the fabrication step, some weak connections and sharp parts in the antenna body are manually improved, and a hole is drilled into the DRA structure for the coaxial probe. Adding bridges at weak connection parts and filleting sharp parts did not affect antenna performance, whereas the air gap between the probe and antenna structure sensitively affected the reflection

coefficient. The antenna was not printed in practice due to COVID-19. The simulation result shows the antenna has fine performances in decoupling, matching and radiation efficiency while it has a narrow bandwidth and large size.

4.1.1 Contributions

- Provided important guidance for the limiting performance of a DRA. In particular, the bandwidth and resonant frequency, are shown to be bounded depending on the materials and superstructure circumscribing the antenna. In this perspective, by providing the limits of these two key parameters, the paper aids researchers to choose DRA's specification such as size, permittivity at the initial step of the design. Although the thesis only provides specific calculations for selected scenario, this concept applies to different permittivity and shape of DRA.
- Conducted a novel optimization for efficient shape synthesis of an arbitrary MIMO DRA. It applies a recent design (*shape-first feed-next*) methodology previously used for microstrip antennas to DRAs and combines it with a decoupling feeding network. This shape synthesis method is relatively flexible compared to the traditional methods and this result shows that it can be applied to DRAs as well as microstrip antennas.
- Proposed a design flow for MIMO DRAs. A detailed procedure for matching, decoupling and preparing complex DRAs for fabrication is provided in this thesis. These results provide an efficient design method for future researchers.

4.2 Future Direction

This chapter suggests some directions for future works and limitations of the thesis.

Chapter 2 addresses lower bounds of the Q factor and the resonant frequency only below the first resonance since all characteristic modes are capacitive in that range. It implies Q factor after the first resonance can be lowered by combining inductive and capacitive modes. Some simulations were carried out and the results showed DRA substructures having a lower Q-factor than the complete structure above the first resonance. Based on this, finding the optimal Q-factor and the resonant frequency of DRA will be interesting for future work.

In Chapter 3, one pair(balanced) of slots are used for port 1 with the Wilkinson divider. In the process, the simulation results show the balanced slots have a better coupling result than the single slot. It implies we can improve the coupling results of three coaxial probes by making each balanced. This feeding technique is not addressed in the thesis, however, it would be worth it for the future task because the coaxial feeding takes less space in x-y plane than the slot feeding with microstrip line.

One limitation is the thesis is finished without fabrication and a measurement result process in practice. Even though the minimum printable size is $20\mu m$, we cannot guarantee the DRA structure is accurately printed since the 3D printing technique has deviations and some parts are still sharp. Some sharp edges and vertices would be printed with errors, and there will be differences between the measured result and the simulated result. The hole for the coaxial probe is very sensitive and even a small error will affect the matching result critically. Therefore, the actual printed structure and measurement data are required in the future. It will give feedback and insight for choosing both the tetrahedron size of the structure and the hole for the probe based on the printable size.

REFERENCES

[1] Richtinger, R.D., "Dielectric Resonators," Journal of Applied Physics , Vol. 10, pp. 391-398, June 1939.

[2] Okaya, A., and L.F. Barash, "The Dielectric Microwave Resonator," Proceedings of the IRE , Vol. 50, Oct. 1962, pp. 2081-2092.

[3] A. Petosa, Dielectric Resonator Antenna Handbook, Norwood, MA, Artech House, 2007.

[4] X.S.Fang, K.W.Leung and K.M.Luk, “Theory and Experiment of Three-Port Polarization-Diversity Cylindrical Dielectric Resonator Antenna”, ” IEEE Transactions on Antennas & Propagation, Vol.62, No.10, pp.4945-4951, Oct.2014

[5] M. W. McAllister, S. A. Long, and G. L. Conway, “Rectangular dielectric resonator antenna,” in Proceedings of the International Symposium Digest—Antennas and Propagation, vol. 21, pp. 696–699, May 1983.

[6] K.-L. Wong, N.-C. Chen, and H.-T. Chen, “Analysis of a Hemispherical dielectric resonator antenna with an airgap,” IEEE Microwave and Guided Wave Letters, vol. 3, no. 10, pp. 355–357, 1993.

[7] Kishk, A.A., "A Triangular Dielectric Re sonator Antenna Excited by a Coaxial Probe," Microwave Optical Technology Letters , Vol. 30, No.5, Sept. 2001, pp. 340-341.

[8] K.Schab, B.Yang, B.Hughs and J.J.Adams “ Lower Bounds on Substructure Antenna Q-Factor”, IEEE transaction on antennas and propagation, vol.66, No.7, July 2018.

[9] B.Yang, J.Kim, J.J.Adams, “Physical Limits on Dielectric Resonator Antennas”, in review.

[10] K.M. Luk and K.W Leung, Dielectric Resonator Antenna, Hertfordshire,England, Research Studies Press LTD, 2003.

[11] R.K. Mongia, A. Ittipiboon, M. Cuhaci, "Measurements of Radiation Efficiency of Dielectric Resonator Antennas," Microwave and Guided Wave Letters, Vol. 4, No. 3, Mar. 1994, pp. 80-82.

[12] A. Ittipiboon, R. K. Mongia, Y. M. M. Antar, P. Bhartia and M. Cuhaci, “Aperture-fed rectangular and triangular dielectric resonators for use as magnetic dipole antennas,” Electron. Lett., vol. 29, pp. 2001-2002, Nov.1993

[13] K. W. Leung, K. M. Luk and E. K. N Yung, "Spherical cap dielectric resonator antenna using aperture coupling," Electron. Lett., vol. 30, No.17, pp. 1366-1367, Aug. 1994

[14] K. Y. Chow and K. W. Leung, “Theory and experiment of the cavity-backed slot-excited dielectric resonator antenna,” IEEE Trans. Electromagnetic Compatibility, vol. 42, No. 3, pp. 290-297, Aug. 2000

[15] K. Y. Chow, K. W. Leung, K. M. Luk and E. K. N. Yung, “Input impedance of the slot-fed dielectric resonator antenna with/without a backing cavity,” IEEE Trans. Antennas Propagat., vol. 49, No. 2, pp.307-309, Feb. 2001

[16] K. W. Leung, K. Y. Chow, K. M. Luk and E. K. N. Yung, “Excitation of dielectric resonator antenna using a soldered-through probe,” Electron. Lett., vol. 33, pp. 349 - 350, Feb. 1997

[17] H. Y. Lo, K. W. Leung and K. M. Luk, “Slotline excited equilateral triangular dielectric resonator antenna of very high permittivity,” Microw. and Opt. Techn. Lett., vol. 29, No. 4, pp. 230-231, Apr. 2001

[18] G. J. Foschini and M. J. Gans, “On limits of wireless communications in a fading environment when using multiple antennas," Wireless personal communications, vol. 6, no. 3, pp. 311-335, 1998.

[19] E. Telatar, “Capacity of multi-antenna gaussian channels," European transactions on telecommunications, vol. 10, no. 6, pp. 585-595, 1999.

[20] Biglieri, E. Calderbank, R. Constantinides, A. Goldsmith, A. Paulraj, A. Poor, H. Vincent. MIMO Wireless Communications. Cambridge University Press. 2007

[21] L. J. Chu, “Physical limitations of omni-directional antennas," Journal of applied physics, vol. 19, no. 12, pp. 1163-1175, 1948.

[22] J. L. Allen and B. L. Diamond, “Mutual Coupling in Array Antennas,” Lincoln Laboratory, M.I.T., Lexington, MA, Tech. Rep. 424(ESD-TR-66-443), 1966.

[23] L. Kundu, “Information-theoretic limits on mimo antennas," Ph.D. dissertation, North Carolina State University, 2016.

[24] X.Chen, M, Abdullah, Q.Li, S.Zhu, H.Shi, A.Zhaan, “Does Low Mutual Coupling Imply Low Antenna Correlation?”, 2019 IEEE International Symposium on Antennas and Propagation and USNC-URSI Radio Science Meeting, Jul 2019

[25] S.-C. Chen, Y.-S. Wang, and S.-J. Chung, “A decoupling technique for increasing the port isolation between two strongly coupled antennas," IEEE Transactions on Antennas and Propagation, vol. 56, no. 12, pp. 3650-3658, Dec 2008.

[26] J. C. Coetzee and Y. Yu, “Design of decoupling networks for circulant symmetric antenna arrays," IEEE Antennas and Wireless Propagation Letters, vol. 8, pp.291-294, 2009.

[27] D. Nie, B. M. Hochwald, E. Stauffer, “Systematic Design of Large-Scale Multiport Decoupling Networks” IEEE Transactions on Circuits and Systems. Vol. 61, pp.2172-2181, Jul.2014

[28] F. Yang and Y. R. Samii, “Microstrip antennas integrated with electromagnetic band-gap EBG structures: A low mutual coupling design for array applications,” IEEE Trans. Antennas Propag., vol. 51, no. 10, pp.2936–2946, Oct. 2003.

[29] Z. Iluz, R. Shavit, and R. Bauer, “Microstrip antenna phased array with electromagnetic bandgap substrate,” IEEE Trans. Antennas Propag, vol. 52, no. 6, pp. 1446–1453, Jun. 2004.

[30] B. K. Lau and J. B. Andersen, “Simple and efficient decoupling of compact arrays with parasitic scatterers," IEEE Transactions on Antennas and Propagation, vol. 60, no. 2, pp. 464-472, 2012.

[31] J. Nasir, M. H. Jamaluddin, M. Khalily, M. R. Kamarudin, I. Ullah, and R. Selvaraju, “A reduced size dual port MIMO DRA with high isolation for 4G applications,” Int. J. RF Microw. Comput.-Aided Eng., vol. 25, pp. 495–501, 2015.

[32] J. Nasir, M. H. Jamaluddin, M. Khalily, M. R. Kamarudin, and I. Ullah, “Design of an MIMO dielectric resonator antenna for 4G applications,” Wireless Pers. Commun., vol. 88, pp. 525–536, 2016.

[33] A. Sharma, G. Das, and R. K. Gangwar, “Dual polarized triple band hybrid MIMO cylindrical dielectric resonator antenna for LTE2500/WLAN/WiMAX applications,” Int. J. RF Microw. Comput.-Aided Eng., vol. 26, pp. 763–772, 2016.

[34] A. A. Khan, M. H. Jamaluddin, S. Aqeel, J. Nasir, J. R. Kazim, and O. Owais, “A dual-band MIMO dielectric resonator antenna for WiMAX/WLAN applications,” Microw., Antenna Propag, vol. 11, pp. 113–120, 2017.

[35] H. Tang, J.X.Chen, W.W. Yang, L.H.Zhou, W.Li “Differential Dual-Band Dual-Polarized Dielectric Resonator Antenna” IEEE Transactions on Antennas and Propagation, Vol.65, pp.855-860, Feb 2017.

[36] X. R. Tang, S. S. Zhong, L. B. Kuang, and Z. Sun, “Dual-polarised dielectric resonator antenna with high isolation and low cross-polarisation,” Electron. Lett., vol. 45, no. 14, pp. 719–720, Jul. 2009.

[37] R.Tian, V.Plicanic, B.K.Lau, Z.Ying “A Compact Six-Port Dielectric Resonator Antenna Array : MIMO Channel Measurement and Performance Analysis” IEEE Transaction on Antennas Propagation., vol. 58, no. 4, pp. 1369–1379, Apr 2010.

[38] A.Abdalrazik, S.El-Hameed and A.Abdel-Rahman, “A Three-Port MIMO Dielectric Resonator Antenna Using Decoupled Model” IEEE Antennas and Wireless Propagation Letters, Vol.16, pp.3104-3107, Oct 2017.

[39] K. Ishimiya, Z. N. Ying, and J. I. Takada, “A compact MIMO DRA for 802.11n application,” in Proc. IEEE AP-S Int. Symp, pp.1–4. Jul. 2008.

[40] A. Savini, G.G. Savini, “A short History of 3D Printing : a Technological Revolution Just Started”, 2015 ICOHTEC/IEEE International History of High-Technologies and their Socio-Cultural Contexts Conference (HISTELCON), Aug 2015.

[41] P. Kumar, S. Dwari, Utkarsh, S. Singh, and J. Kumar, “Investigation and development of 3D printed biodegradable PLA as compact antenna for broadband applications," IETE Journal of Research, 2018.

[42] P. Nayeri, M. Liang, R.S.Garcia, M.Tuo, F.Yang, M.Gehm, H.Xin, “High Gain Dielectric Reflectarray Antennas for THz application”, 2013 IEEE Antennas and Propagation Society International Symposium, Jul 2013.

[43] J.Kim, D.Shin, S.Choi, D.Yoo, I. Seo, K. Kim “Meta-lens design with low permittivity dielectric materials through smart transformation optics”, Applied Physics Letters, vol.107, no.10, Aug 2015.

[44] C. M. Shemelya, M. Zemba, C. Kief, D. Espalin, R.B. Wicker, E. MacDonald “Multi-Layer Off-Axis Patch Antennas Fabricated Using Polymer Extrusion 3D printing” 2016 10th European Conference on Antennas and Propagation (EuCAP), Apr 2016

[45] J.Huang, S.J.Chen, Z.Xue, W.Withayachumnankul, C.Fumeaux, “Impact of infill pattern on 3D_printed Dielectric Resonator Antennas”, 2019 IEEE Asia-Pacific Conference on Antennas and Propagation, Aug 2018

[46] Qi Wu, “Dielectric Resonator Antennas by Low Cost 3D Printing : Characteristic Mode Approach”, 2019 IEEE International Conference on Computational Electromagnetics, Mar 2019

[47] V.Marrocco, V.Basile, I.Fassi, M.Grande, D.Laneve, F.Prundenzano, A.D'Orazio, "Dielectric Resonant Antennas via Additive Manufacturing for 5G Communications", 2019 Photonics&Electromagnetics Research Symposium, Jun 2019

[48] H. Alroughani and D.A.McNamara, " The Shape synthesis of Dielectric Resonator Antennas" IEEE Transactions on Antennas & Propagation, Vol.68, pp.5766-5777. Aug.2020

[49] N.Travitzky, A.Bonet, B. Dermeik, T.Fey, I. F. Demut,, L. Schlier, T. Schlordt, P.Greil, "Additive Manufacturing of Ceramic-Based Materials", Advanced Ceramics and Coating Processing, vol.16, pp.729-754, Jun 2014

[50] Y. Oh, V. T. Bharambe, B. Mummareddy, J. Martin, J. McKnight, M. Abraham, J. Walker, K. Rogers, B. Conner, P. Cortes, E. MacDonald, and J. J. Adams, "Microwave Dielectric Properties of Zirconia Fabricated using NanoParticle Jetting," Additive Manufacturing, Mar. 2019.

[51] N. Delhote, D.Ballargeat, S.Verdeyme, C.Delage, C.Chaput, "Ceramic Layer-by-Layer Stereolithography for the Manufacturing of 3-D Millimeter-Wave Filters", IEEE Transactions on Antennas and Propagation, vol.55, no.3, Mar 2007.

[52] R. Garbacz and R. Turpin, "A generalized expansion for radiated and scattered fields," IEEE Transactions on Antennas and Propagation, vol. 19, no. 3, pp. 348-358, 1971.

[53] R. Harrington and J. Mautz, "Theory of characteristic modes for conducting bodies," IEEE Transactions on Antennas and Propagation, vol. 19, no. 5, pp. 622-628, 1971.

[54] R. F. Harrington, Field Computation by Moment Methods. Wiley - IEEE Press, 1993.

[55] G. A. E. Vandenbosch, "Reactive Energies, Impedance, and Q Factor of Radiating Structures," in IEEE Transactions on Antennas and Propagation, vol. 58, no. 4, pp. 1112-1127, April 2010.

[56] B.Yang and J.J.Adams, "Quality Factor Calculations for the Characteristic Modes of Dielectric Resonator Antennas", 2017 United States National Committee of URSI National Radio Science Meeting, Mar 2017.

[57] H. Alroughani, J. L. T. Ethier, and D. A. McNamara, "Observations on computational outcomes for the characteristic modes of dielectric objects," in 2014 IEEE Antennas and Propagation Society International Symposium (APSURSI), July 2014, pp. 844–845.

[58] Z. T. Miers and B. K. Lau, “Computational analysis and verifications of characteristic modes in real materials,” IEEE Transactions on Antennas and Propagation, vol. 64, no. 7, pp. 2595–2607, 2016.

[59] M.Gustafsson, D.Tayli, C.Ehrenborg, M.Cismasu, S.Nordebo, “Antenna Current Optimization using MATLAB and CVX”, Forum for Electromagnetic Research Methods and Application Technologies, pp. 1-29, Aril, 2017

[69] D. Schaubert, D. Wilton and A. Glisson, "A tetrahedral modeling method for electromagnetic scattering by arbitrarily shaped inhomogeneous dielectric bodies," in IEEE Transactions on Antennas and Propagation, vol. 32, no. 1, pp. 77-85, Jan 1984.

[61] R. L. Haupt, D. H.Werner, “Genetic Algorithms in Electromagnetics”, Wiley Interscience, 2007

[62] J. M. Johnson, Y.R.Samil, “Genetic Algorithms in Engineering Electromagnetics”, ” IEEE Transactions on Antennas and Propagation, vol.39, pp. 7-21, 1997

[63] J. J. Adams and J. T. Bernhard, “Broadband equivalent circuit models for antenna impedances and fields using characteristic modes,” IEEE Transactions on Antennas and Propagation, vol. 61, no. 8, pp. 3985–3994, 2013.

[64] B.Yang, A.Eroglu, J.J.Adams “Shape Synthesis of Multi-Mode Dielectric Resonator Antennas Using Characteristic Modes”, 2020 International Applied Computational Electromagnetics Society Symposium (ACES), Jul 2020/

[65] B. Yang, J. Zhou, and J. J. Adams, “A shape-first, feed-next design approach for compact planar mimo antennas,” Progress In Electromagnetics Research, vol. 77, pp. 157–165, 2019

[66] “Microstrip Line Calculator,” Microstrip line calculator. [Online]. Available: http://www.emtalk.com/mscalc.php. [Accessed: 15-Mar-2021].

[67] R. G. Vaughan, “Signals in Mobile Communications,” IEEE Transactions on Vehicular Technology, Vol. 35, 1986, pp. 133-145.

[68] V.T.Bharambe, Y. Oh, J.J.Adams “3D Printed Zirconia for UWB Stacked Conical Ring DRA”, 2020 IEEE International Symposium on Antenna and Propagation and North Americal Radio Science Meeting.